electronics

MDPI

Article

Real-Time Aircraft Altitude Estimation for SAR Imaging Using Pitch Sum with Difference Channels and Multi-Beams

Zhichao Zhou *, Naigang Zhao, Wei Wu, Xiaofei He and Bin He

School of Computer and Network Engineering, Shanxi Datong University, Datong 037009, China; 03090125@sxdtdx.edu.cn (N.Z.); 03090063@sxdtdx.edu.cn (W.W.); hexiaofei@sxdtdx.edu.cn (X.H.); aihebin19@sxdtdx.edu.cn (B.H.)
* Correspondence: 03210017@sxdtdx.edu.cn

Abstract

Real-time aircraft altitude estimation is critical for synthetic aperture radar imaging. Altitude errors can cause geometric distortions in ground imagery, such as image rotation and deformation, and degrade target detection and recognition. Conventional aircraft altitude estimation methods often rely on complex hardware or processing chains. This makes them unsuitable for real-time operation on high-speed platforms with complex trajectories. To address this issue, this paper proposes a real-time altitude estimation method based on the pitch sum with difference channels. The method estimates aircraft altitude by analyzing the variation in pitch-angle deviation with the slant range using the sum with difference channel data. Furthermore, to mitigate the impact of grazing-angle errors, sequential and cyclic multi-beams modes are developed. By formulating and solving equations using multi-beams observations at different grazing angles, the grazing-angle error is suppressed, improving the estimation accuracy. The proposed methods are validated through computer simulations and real airborne synthetic aperture radar data. The results demonstrate that the method is effective for real-time altitude estimation in airborne synthetic aperture radar imaging and has practical potential for electronic sensing and radar imaging systems.

Keywords: aircraft altitude estimation; cyclic multi-beams; pitch sum with difference channels; synthetic aperture radar imaging; sequential multi-beams

1. Introduction

Aircraft altitude (relative to the imaging area or target) is a key parameter for characterizing spatial information. It has essential applications in radar control, reconnaissance, and synthetic aperture radar (SAR) [1–3] imaging. In military operations, the aircraft's altitude aids in obtaining location-based information to precisely locate enemy targets. This provides a concrete foundation for follow-up observation, tracking and attack against the target. In civil applications, aircraft altitude measurement is used to survey unknown terrains, such as submarine topography or glacier sea altitude, thereby facilitating various human activities.

Synthetic aperture radar is an imaging radar that provides two-dimensional, high-resolution image of the illuminated area, with all-weather and all-time observation capabilities. Most SAR imaging algorithms include a geometric correction step (projecting the slant-range image onto the ground-range image) [4]. The main purpose of this step is to remove the geometric distortions of the slant-range image and obtain the true geometric information of the feature. Therefore, aircraft altitude is a critical parameter for this step.

Check for updates

Academic Editor: George Angelos Papadopoulos

Received: 3 October 2026
Revised: 22 October 2026
Accepted: 25 October 2026
Published: 29 October 2026

Copyright: © 2026 by the authors. Licensee MDPI, Basel, Switzerland. This article is an open access article distributed under the terms and conditions of the Creative Commons Attribution (CC BY) license.

Inaccurate aircraft altitude leads to residual geometric distortion in the ground-range image. Most publications on aircraft parameter estimation only focus on velocity, acceleration or motion error [5,6]. Although some studies [7–9] discuss the variation in the Doppler centroid with range, none involve altitude estimation.

There are two main methods to directly obtain an aircraft's altitude: one relies on the Inertial Navigation System (INS) [10] or Global Positioning System (GPS) [11], and the other uses a radar altimeter. The INS [12] has a higher update rate for measuring aircraft altitude, but it suffers from zero drift [13], meaning the measurement error increases over time. Conversely, GPS does not have the zero drift problem, but its update rate is lower. Therefore, INS and GPS are often integrated to achieve high precision for aircraft altitude and SAR imaging. However, load-limited platforms often cannot accommodate high-precision integrated GPS/INS systems.

A radar altimeter [14,15] is an active measurement device. A traditional radar altimeter transmits narrow pulses directly downward and receives the ground echoes. Aircraft altitude is calculated based on the time delay between the transmitted pulse and the half-power point of the rising edge of the main-lobe echo. At high altitudes, the ground beam becomes considerably large, which degrades measurement accuracy. A SAR altimeter operates in the pulse-Doppler mode, transmitting a series of pulses to the ground. Synthetic aperture processing and delay correction are applied to the echoes to obtain the average echo waveform. The altitude measurement method is similar to that of a traditional radar altimeter. Since a traditional radar altimeter only utilizes the echo energy within the limited pulse footprint, the remaining energy in the beam is wasted. The SAR altimeter overcomes this by utilizing all the beam energy to increase the number of effective observations and improve the measurement accuracy.

On the other hand, due to servo platform constraints, the SAR antenna is often unable to point directly downward. Therefore, a separate altitude measurement antenna must be installed for the radar altimeter, which significantly increases system complexity. Furthermore, the radar altimeter only measures the altitude directly beneath the platform. When SAR operates in squint mode (i.e., an acute angle between the beam-pointing and platform's velocity directions) with a relatively large beam-center slant range, significant differences may exist between the altitude of the illuminated area and the area directly below the platform. Consequently, this inevitable altitude error degrades geometric correction accuracy, rendering the direct use of an altimeter for aircraft altitude measurement ineffective.

An adaptive aircraft altitude estimation method based on squint data was proposed in [16]. This method indirectly estimates altitude by extracting the variation in the Doppler center with the slant range. However, it is inapplicable to broadside or diving modes, and its measurement accuracy is highly sensitive to non-uniform scene scattering. Aircraft altitude can also be estimated using autofocusing [17,18] or phase calibration [19,20]. These methods typically require one or multiple images and use iterative processing to estimate altitude-related errors or the altitude itself. Consequently, their estimation accuracy depends on image focusing quality, making them unsuitable for real-time processing, especially for high-speed diving SAR [21,22]. Using narrow-beam antennae, altimetry strategies such as interferometric SAR techniques based on interferometric phase differences [23] have also been proposed. However, these methods rely on platform attitude information, making accurate altitude estimation difficult when the attitude is unknown.

To address these issues, this study proposes an adaptive real-time method for aircraft altitude estimation based on the pitch sum with difference channel data. The method estimates aircraft altitude by analyzing the variation in the pitch angle deviation with the slant range. The beam-center slant range and grazing angle are determined by locating the zero-depth position of the difference channel. Then, the aircraft altitude is estimated based

on the geometric relationship. On this basis, the sequential and cyclic multi-beam methods are proposed to mitigate the impact of angle errors on altitude measurement accuracy. These multi-beams methods rely on the relative variations in aircraft altitude and grazing angle between beams, which are provided by the INS.

A closely related method was proposed by Li et al. [24], who established the basic framework of using the multi-beam pitch sum with difference channels for aircraft altitude estimation under oblique irradiation. Their work demonstrated that the pitch sum with the difference angle measurement principle can achieve accurate beam-center slant range estimation. Furthermore, the cyclic multi-beam mode can estimate grazing-angle deviations, thereby enabling altitude estimation even when the beam cannot be directed vertically downward. The present work builds upon this framework and extends it in several important directions. A terrain-undulation perturbation model is established to analyze how surface elevation variations disturb the relationship between the pitch-angle deviation and the slant range. The error propagation is reformulated using the full covariance matrix, explicitly retaining the correlations among the fitting coefficients and the cross-covariance between the slant range and the grazing angle. Then, the performance under different curve-fitting orders is quantitatively compared. The second-order fit is justified by both accuracy and computational cost. The sensitivity to the prior ground-footprint elevation error and the accumulation of INS relative errors are analyzed. The effect of patch-to-patch scattering differences in the cyclic mode is modeled, and weighted least squares is introduced to mitigate the influence of weak-scattering patches. Finally, analytical beam-position design formulae are derived, replacing the empirical trial-and-error approach based on simulation curves. These extensions make the proposed method more comprehensive and better suited for practical airborne SAR applications than the original framework.

The work is organized as follows: Section 2 presents the adaptive aircraft altitude estimation method based on the pitch sum with difference channels, and analyzes its estimation accuracy. Section 3 presents the adaptive aircraft altitude estimation based on the multi-beam mode. It introduces the multi-beam operation and focuses on the estimation accuracy and beam-position design criteria. Section 4 presents the results, verifying the estimation performance of the proposed algorithm through simulations and real data. Section 5 discusses the practical interpretations and limitations of the proposed methods. It also compares the applicability of different approaches and outlines future research directions. Finally, Section 6 concludes the paper.

2. Aircraft Altitude Estimation Based on Pitch Sum with Difference Channels

2.1. Principle and Process

The adaptive aircraft altitude estimation based on the pitch sum with difference channels requires the radar to receive echoes from these channels and to measure the grazing angle of each range cell relative to the beam center. Figure 1 illustrates the geometric mode of this method. The aircraft altitude is denoted as H. The slant range and grazing angle corresponding to the beam center are R_{ref} and β_{ref}, respectively. For the nth range cell, the corresponding slant range and grazing angle are R_n and β_n, and the pitch-angle deviation relative to the beam center is ξ_n.

From the geometry shown in Figure 1, the relationship can be expressed as follows.

$$\xi_n = \arcsin\left(H/R_{ref}\right) - \arcsin(H/R_n)\ . \tag{1}$$

Equation (1) assumes that the ground footprints of the beam center and the nth range cell have the same surface elevation. In practice, surface undulations disturb the relationship between the pitch-angle deviation and the slant range. Let $h_{g,ref}$ and $h_{g,n}$ denote the ground

elevations at the beam center and the nth range cell, respectively. Define the terrain elevation disturbance as $\Delta h_n = h_{g,n} - h_{g,ref}$. Therefore, the geometric relationship in (1) is modified as follows.

$$\xi_n = \arcsin\left(H/R_{ref}\right) - \arcsin[(H - \Delta h_n)/R_n]. \tag{2}$$

For small Δh_n, the first-order Taylor expansion of (2) around $\Delta h_n = 0$ yields

$$\xi_n \approx \xi_n^{(0)} + \Delta h_n/(R_n \cos\beta_n)\ , \tag{3}$$

where $\xi_n^{(0)}$ is the pitch-angle deviation given by (1) under the flat-ground assumption. The terrain-induced pitch-angle error is given by

$$\xi_n \approx \xi_n^{(0)} + \Delta h_n/(R_n \cos\beta_n)\ . \tag{4}$$

Equation (4) shows that the terrain-induced angle error is proportional to the elevation variation. It is also inversely proportional to the slant range and the cosine of the grazing angle.

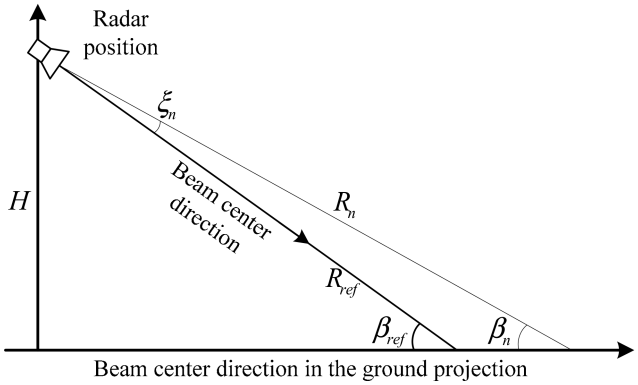


Figure 1. Geometric model of the adaptive aircraft altitude estimation based on pitch sum with difference channels.

As can be seen from the equations above, the variation in ξ_n with R_n depends on the aircraft altitude H. Specifically, over the same slant range interval, the variation pattern of ξ_n changes with different altitudes. Therefore, this property can be exploited to estimate the aircraft altitude.

The specific steps of the adaptive aircraft altitude estimation based on the pitch sum with difference channels are as follows:

The first step is to measure the pitch angle using the sum and difference channel echoes. Range pulse compression is applied to the echoes from both channels. The angle is then measured from the echo of the corresponding range cell using the amplitude or phase comparison. This yields the pitch-angle deviation of the range cell relative to the beam center. Taking the amplitude-comparison angle measurement as an example, let s_n and d_n denote the sum and difference channel signals of the nth range cell after range pulse compression, respectively. The measured angle is calculated as follows:

$$\xi_n = \frac{1}{k_{slope}} \mathrm{Re}\left(\frac{d_n}{s_n}\right), \tag{5}$$

where k_{slope} is the difference slope of the pitch difference channel antenna pattern, and $\mathrm{Re}(\cdot)$ represents the real part of the complex signal.

The second step is to estimate the beam-center slant range. According to (1), $\xi_n = 0$ when $R_n = R_{ref}$. Therefore, the beam-center slant range can be found by locating the zero-crossing point where $\xi_n = 0$. To suppress noise, curve fitting is applied to ξ_n. Using

a quadratic polynomial fit as an example, we assume that, near $\xi_n = 0$, the variation in ξ_n with R_n can be expressed as follows:

$$\xi_n = aR_n^2 + bR_n + c\ . \tag{6}$$

Using the least squares criterion, we can estimate the quadratic curve coefficients $\hat{a}$, $\hat{b}$, and $\hat{c}$. The beam-center slant range is then determined by solving for the root where $\xi_n = 0$:

$$\hat{R}_{ref} = \frac{-\hat{b} + \sqrt{\hat{b}^2 - 4\hat{a}\hat{c}}}{2\hat{a}} \text{ or } \hat{R}_{ref} = \frac{-\hat{b} - \sqrt{\hat{b}^2 - 4\hat{a}\hat{c}}}{2\hat{a}}. \tag{7}$$

Since the equation yields two roots, one must be eliminated based on the physical geometry. If the pitch difference channel is formed by subtracting the lower antenna echo from the upper antenna one, ξ_n increases with R_n. In this case, the first root is selected; otherwise, the second root is chosen. Without loss of generality, the first root is assumed to be correct here.

The third step is to estimate the beam-center grazing angle. Differentiating ξ_n in (1) with respect to R_n and evaluating it at $R_n = R_{ref}$ yields the slope (8):

$$k_{ref} = \left.\frac{d\xi_n}{dR_n}\right|_{R_n = R_{ref}} = \frac{1}{R_{ref}}\tan\left(\beta_{ref}\right). \tag{8}$$

Furthermore, terrain disturbances affect the slope of the pitch-angle deviation with respect to slant range. The terrain-induced slope perturbation can be approximated as

$$\delta k_{ref} \approx \frac{\left(dh_{g,n}/dR_n\right)}{R_n\cos\beta_n} - \frac{\Delta h_n}{R_n^2\cos\beta_n} + \frac{\Delta h_n \tan\beta_n}{R_n\cos\beta_n}\frac{d\beta_n}{dR_n}\ , \tag{9}$$

where $dh_{g,n}/dR_n$ is the local terrain slope. Equation (9) shows that the terrain slope is the main perturbation source: gentle undulations mainly cause random errors, whereas steep slopes cause systematic slope bias.

Based on the fitted curve from the second step, the estimated slope can be obtained:

$$\hat{k}_{ref} = \sqrt{\hat{b}^2 - 4\hat{a}\hat{c}}. \tag{10}$$

Therefore, the beam-center grazing angle is calculated as follows:

$$\hat{\beta}_{ref} = \arctan\left(\hat{k}_{ref}\hat{R}_{ref}\right)\ . \tag{11}$$

The fourth step is to estimate the aircraft altitude. Based on the geometric relationship, the aircraft altitude is calculated as follows:

$$\hat{H}_{ref} = \hat{R}_{ref}\sin\left(\hat{\beta}_{ref}\right)\ . \tag{12}$$

The overall estimation flowchart is shown as Figure 2:

2.2. Estimation Accuracy

Based on the principle of error propagation, the estimation accuracy analysis is divided into four parts. First, the accuracy of the pitch angle ξ_n is analyzed, followed by the curve fitting coefficients $\hat{a}$, $\hat{b}$, and $\hat{c}$. Then, the accuracy of the beam-center slant range $\hat{R}_{ref}$ and grazing angle $\hat{\beta}_{ref}$ is evaluated. Finally, the accuracy of the aircraft altitude is determined.

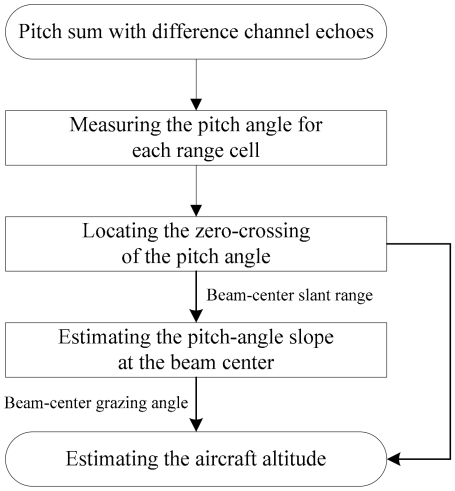


Figure 2. Flowchart of the adaptive aircraft altitude estimation based on pitch sum with difference channels.

2.2.1. Pitch Angle Accuracy

Sherman et al. [25] thoroughly discussed the principles and methods of sum and difference channel angle measurement, providing formulae for calculating the angle deviation and variance. Therefore, this section focuses on the impact of angle deviation on altitude estimation and the corresponding correction method.

As analyzed in [25], the angle measurement accuracy for fluctuating targets is lower than that for stable targets, resulting in a larger angle deviation, which is expressed as follows:

$$B_{\hat{\xi}_n} = -\frac{\xi_n}{\mathrm{SNR}+1}, \tag{13}$$

where ξ_n denotes the true angle value and SNR represents the signal-to-noise ratio.

The corrected pitch angle is calculated as follows:

$$\xi_n^{corr} = \xi_n - B_{\hat{\xi}_n}. \tag{14}$$

The SNR in (13) is estimated from the range-compressed sum and difference channel data as follows: The signal energy is estimated by averaging the sum-channel energy over the selected range cells, and the noise energy is estimated from the difference-channel energy in the zero-depth region, where the angle response is approximately zero. This echo-based SNR estimation is adopted because it automatically accounts for actual scene backscatter, system noise, and channel gain. Therefore, it is more suitable for airborne SAR data than using nominal system parameters alone.

Besides the noise-induced angle bias in (13), the terrain undulation analyzed in Section 2.1 introduces an additional angle error. Based on (4), the standard deviation of the terrain-induced angle error can be expressed as follows:

$$\sigma_{\xi_n,\mathrm{terrain}} \approx \frac{\sigma_{h_g}}{R_n \cos\beta_n}, \tag{15}$$

where σ_{h_g} represents the standard deviation of the ground-footprint elevation prior error. Therefore, the total angle error variance becomes

$$\sigma_{\hat{\xi}_n}^2 = \sigma_{\hat{\xi}_n,\mathrm{noise}}^2 + \sigma_{\hat{\xi}_n,\mathrm{terrain}}^2 . \tag{16}$$

The noise-induced variance $\sigma_{\hat{\xi}_n,\mathrm{noise}}^2$ is obtained from the Sherman formula (13) and the estimated SNR. In contrast, the terrain-induced variance is calculated from (15) using an available digital elevation model or the statistical surface roughness of the observation area.

The correction in (14) only compensates for the angle bias induced by noise and energy fluctuations, which corresponds to the component $\sigma_{\xi_n,\text{noise}}$ in (16). The terrain-induced component $\sigma_{\xi_n,\text{terrain}}$ cannot be removed by (14); rather, it is handled by the terrain-corrected geometric model in (2) and the elevation prior in (15). Therefore, the total angle error after correction becomes

$$\sigma^2_{\xi_n,\text{corr}} = \sigma^2_{\xi_n,\text{noise,corr}} + \sigma^2_{\xi_n,\text{terrain}}, \tag{17}$$

where $\sigma_{\xi_n,\text{noise,corr}}$ is the residual noise-induced error after applying (14). In the following verification, the two components are evaluated separately to clearly assess the correction effect.

In the pitch sum with difference channel aircraft altitude estimation, the echo of each range cell is formed by the coherent superposition of numerous scatterers, causing inevitable energy fluctuations. In practice, it is necessary to correct the angle measurement based on (13). The SNR can be calculated from system parameters or estimated from echo statistics. When estimated from echoes, the signal energy is determined by the sum-channel energy, while the noise energy is extracted from the difference-channel energy near the zero depth.

Furthermore, to reduce the variance in the angle measurement, a weighted average can be applied across multiple range cells. The weights are set proportional to the sum-channel signal energy of the corresponding range cells.

2.2.2. Accuracy of Curve Fitting Coefficients

Equation (6) for all range cells can be expressed as a matrix form, that is,

$$\boldsymbol{\Psi} = \mathbf{R}\boldsymbol{\Theta}, \tag{18}$$

where

$$\boldsymbol{\Psi} = \begin{bmatrix} \xi_1 \\ \xi_2 \\ \vdots \\ \xi_N \end{bmatrix}, \ \mathbf{R} = \begin{bmatrix} R_1^2 & R_1 & 1 \\ R_2^2 & R_2 & 1 \\ \vdots & \vdots & \vdots \\ R_N^2 & R_N & 1 \end{bmatrix}, \ \boldsymbol{\Theta} = \begin{bmatrix} a \\ b \\ c \end{bmatrix}. \tag{19}$$

Here, N represents the total number of range cells. Using the least squares criterion, the estimated quadratic curve coefficients in (6) are as follows:

$$\hat{\boldsymbol{\Theta}} = \left(\mathbf{R}^{\mathrm{T}}\mathbf{R}\right)^{-1}\mathbf{R}^{\mathrm{T}}\boldsymbol{\Psi}. \tag{20}$$

The three elements of $\hat{\boldsymbol{\Theta}}$ correspond to the estimated values of $\hat{a}$, $\hat{b}$, and $\hat{c}$, respectively:

$$\hat{a} = \hat{\boldsymbol{\Theta}}_1, \ \hat{b} = \hat{\boldsymbol{\Theta}}_2, \ \hat{c} = \hat{\boldsymbol{\Theta}}_3. \tag{21}$$

Since slant range measurements are generally more accurate, the error in $\hat{\boldsymbol{\Theta}}$ primarily originates from ξ. Because the three fitting coefficients are jointly estimated via least squares, their estimation errors are generally correlated. Therefore, error propagation should be performed using the full covariance matrix rather than assuming independent variables.

Based on (20), the estimation error of $\hat{\boldsymbol{\Theta}}$ is

$$\boldsymbol{\delta}\hat{\boldsymbol{\Theta}} = \left(\mathbf{R}^{\mathrm{T}}\mathbf{R}\right)^{-1}\mathbf{R}^{\mathrm{T}}\boldsymbol{\delta\Psi}, \tag{22}$$

where $\boldsymbol{\delta\Psi} = [\delta\xi_1, \ldots, \delta\xi_N]^{\mathrm{T}}$ is the angle error vector. The covariance matrix of $\hat{\boldsymbol{\Theta}}$ is

$$\mathbf{C}_{\boldsymbol{\Theta}} = \left(\mathbf{R}^{\mathrm{T}}\mathbf{R}\right)^{-1}\mathbf{R}^{\mathrm{T}}\mathbf{C}_{\xi}\mathbf{R}\left(\mathbf{R}^{\mathrm{T}}\mathbf{R}\right)^{-1}, \tag{23}$$

where $\mathbf{C}_{\xi} = \mathbf{E}\left[\boldsymbol{\delta\Psi}\boldsymbol{\delta\Psi}^{\mathrm{T}}\right]$ is the covariance matrix of the angle errors. The diagonal elements of $\mathbf{C}_{\xi}$ are the total angle error variances given by (16), i.e., $\left[\mathbf{C}_{\xi}\right]_{nn} = \sigma^2_{\xi_n} = \sigma^2_{\xi_n,\text{noise,corr}} + \sigma^2_{\xi_n,\text{terrain}}$. If the angle errors of different range cells are mutually independent, $\mathbf{C}_{\xi}$ is diagonal;

if the terrain or clutter introduces spatial correlation, the off-diagonal elements of $\mathbf{C}_{\tilde{\xi}}$ should be retained.

If all range cells share the same angle error variance $\sigma^2_{\tilde{\xi}_n}$ and are mutually independent, (23) reduces to

$$\mathbf{C}_{\hat{\boldsymbol{\theta}}} = \sigma^2_{\tilde{\xi}_n} \left(\mathbf{R}^{\mathrm{T}}\mathbf{R}\right)^{-1}. \tag{24}$$

In general, $\mathbf{C}_{\hat{\boldsymbol{\theta}}}$ is a full 3 × 3 matrix, and its off-diagonal elements represent the correlations between $\hat{a}$, $\hat{b}$, and $\hat{c}$. These correlations must be retained in the subsequent error propagation.

2.2.3. Effect of the Fitting Order

The fitting order determines how well the polynomial approximates the theoretical arcsine relation and how sensitive the estimation is to noise. In this subsection, the first-, second-, and third-order models are compared in terms of the fitting residual, the estimated beam-center slant range $\hat{R}_{ref}$, the estimated grazing angle $\hat{\beta}_{ref}$, and the final altitude error.

For each fitting order, the beam-center slant range is obtained by solving $\xi_n = 0$. For the first-order model, the solution is

$$\hat{R}^{(1)}_{ref} = -\frac{\hat{c}}{\hat{b}}. \tag{25}$$

For the second-order model, the solution is given by (7). For the third-order model, the root nearest to the beam center is selected among the real roots of the cubic equation.

The slope at the beam center is then calculated from the derivative of the fitted polynomial at $\hat{R}_{ref}$, and the grazing angle and altitude are obtained from (11) and (12), respectively.

The theoretical relation $\xi_n = \arcsin\left(H/R_{ref}\right) - \arcsin(H/R_n)$ exhibits the following properties. Its Taylor expansion around R_{ref} is dominated by the first- and second-order terms when the fitting interval is not too large. Therefore,

- The first-order fit cannot capture the curvature of the arcsine relation. It introduces a systematic slope bias, which propagates to $\hat{\beta}_{ref}$ and $\hat{H}$;
- The second-order fit captures the leading curvature term and provides a good balance between approximation accuracy and noise sensitivity;
- The third-order fit can further reduce the fitting residual, but the higher-order coefficient is more sensitive to angle noise. When the SNR is limited or the fitting interval is short, the third-order fit may overfit the noisy angle curve and amplify the altitude error.

The fitting interval selection is related to the fitting order and to the theoretical curvature of the angle–range relation. In this work, the interval is selected by the following procedure:

1. Theoretical half-window constraint. From the Taylor expansion of $\xi_n(R_n)$ around R_{ref}, the relative contribution of the third-order term to the slope is approximately $(|c_3/c_2|)L$. To keep this contribution below a threshold η_L, the half-window L should satisfy $L \le \eta_L|c_2/c_3|$;
2. Interval centering. The interval is centered at the zero-crossing range cell $R_{i,c} = \arg\min_R |r_i(R)|$, refined by linear interpolation;
3. Symmetric extension and stopping criterion. Starting from $R_{i,c}$, the interval $I_i(L) = \left[R_{i,c} - L, R_{i,c} + L\right]$ is extended symmetrically until one of the following conditions is met: the second-order fitting RMSE exceeds 0.05°; the half-window reaches the theoretical bound L; or the interval reaches a terrain- or scattering-discontinuity cell;
4. Exclusion of discontinuities. Range cells with local terrain slope exceeding the threshold in Section 2.1, or with adjacent-window energy change exceeding 3 dB, are excluded, as discussed in Section 3.1.2.

In summary, the curvature constraint on L is the dominant factor for fitting interval selection.

2.2.4. Slant Range and Grazing Angle Accuracy

Since $\hat{R}_{ref}$ is a function of the correlated fitting coefficients $\hat{a}$, $\hat{b}$, and $\hat{c}$, its variance should be calculated using the full covariance matrix $\mathbf{C}_{\hat{\boldsymbol{\theta}}}$ in (23). Define the gradient vector as

$$g_R = \left[\frac{\partial \hat{R}_{ref}}{\partial \hat{a}}, \frac{\partial \hat{R}_{ref}}{\partial \hat{b}}, \frac{\partial \hat{R}_{ref}}{\partial \hat{c}} \right]^{\mathrm{T}}, \tag{26}$$

where

$$\frac{\partial \hat{R}_{ref}}{\partial \hat{a}} = -\hat{R}_{ref} - \frac{\hat{c}}{\hat{a}\sqrt{\hat{b}^2 - 4\hat{a}\hat{c}}}, \quad \frac{\partial \hat{R}_{ref}}{\partial \hat{b}} = \frac{\hat{b}}{2\hat{a}\sqrt{\hat{b}^2 - 4\hat{a}\hat{c}}} - \frac{1}{2\hat{a}}, \quad \frac{\partial \hat{R}_{ref}}{\partial \hat{c}} = \frac{-1}{\sqrt{\hat{b}^2 - 4\hat{a}\hat{c}}}. \tag{27}$$

Then, the variance of $\hat{R}_{ref}$ is

$$\sigma^2_{\hat{R}_{ref}} = g_R^{\mathrm{T}} \mathbf{C}_{\hat{\boldsymbol{\theta}}} g_R. \tag{28}$$

When $\mathbf{C}_{\hat{\boldsymbol{\theta}}}$ is diagonal, (28) reduces to the original form; otherwise, the off-diagonal terms of $\mathbf{C}_{\hat{\boldsymbol{\theta}}}$ contribute to $\sigma^2_{\hat{R}_{ref}}$ and must not be neglected.

Similarly, the grazing angle $\hat{\beta}_{ref}$ is also a function of $\hat{a}$, $\hat{b}$, and $\hat{c}$. Define the gradient vector as

$$g_\beta = \left[\frac{\partial \hat{\beta}_{ref}}{\partial \hat{a}}, \frac{\partial \hat{\beta}_{ref}}{\partial \hat{b}}, \frac{\partial \hat{\beta}_{ref}}{\partial \hat{c}} \right]^{\mathrm{T}}. \tag{29}$$

where

$$\begin{aligned}
\frac{\partial \hat{\beta}_{ref}}{\partial \hat{a}} &= \frac{1}{1+\hat{k}_{ref}^2 \hat{R}_{ref}^2} \left(-\frac{2\hat{c}}{\sqrt{\hat{b}^2 - 4\hat{a}\hat{c}}} \hat{R}_{ref} + \hat{k}_{ref} \frac{\partial \hat{R}_{ref}}{\partial \hat{a}} \right), \\
\frac{\partial \hat{\beta}_{ref}}{\partial \hat{b}} &= \frac{1}{1+\hat{k}_{ref}^2 \hat{R}_{ref}^2} \left(\frac{\hat{b}}{\sqrt{\hat{b}^2 - 4\hat{a}\hat{c}}} \hat{R}_{ref} + \hat{k}_{ref} \frac{\partial \hat{R}_{ref}}{\partial \hat{b}} \right), \\
\frac{\partial \hat{\beta}_{ref}}{\partial \hat{c}} &= \frac{1}{1+\hat{k}_{ref}^2 \hat{R}_{ref}^2} \left(-\frac{2\hat{a}}{\sqrt{\hat{b}^2 - 4\hat{a}\hat{c}}} \hat{R}_{ref} + \hat{k}_{ref} \frac{\partial \hat{R}_{ref}}{\partial \hat{c}} \right).
\end{aligned} \tag{30}$$

Then, the variance of $\hat{\beta}_{ref}$ is

$$\sigma^2_{\hat{\beta}_{ref}} = g_\beta^{\mathrm{T}} \mathbf{C}_{\hat{\boldsymbol{\theta}}} g_\beta. \tag{31}$$

Moreover, because both $\hat{R}_{ref}$ and $\hat{\beta}_{ref}$ are derived from the same fitting coefficients, they are generally correlated. Their covariance is

$$\mathrm{Cov}\left(\hat{R}_{ref}, \hat{\beta}_{ref}\right) = g_R^{\mathrm{T}} \mathbf{C}_{\hat{\boldsymbol{\theta}}} g_\beta. \tag{32}$$

This covariance term is essential for the altitude error calculation in Section 2.2.5.

2.2.5. Aircraft Altitude Accuracy

Based on the estimated aircraft altitude in (12) and the errors of the beam-center slant range $\hat{R}_{ref}$ and grazing angle $\hat{\beta}_{ref}$, the altitude estimation error is calculated using the complete covariance propagation:

$$\sigma^2_{\hat{H}} = \left(\frac{\partial \hat{H}}{\partial \hat{R}_{ref}} \sigma_{\hat{R}_{ref}} \right)^2 + \left(\frac{\partial \hat{H}}{\partial \hat{\beta}_{ref}} \sigma_{\hat{\beta}_{ref}} \right)^2 + 2 \frac{\partial \hat{H}}{\partial \hat{R}_{ref}} \frac{\partial \hat{H}}{\partial \hat{\beta}_{ref}} \mathrm{Cov}\left(\hat{R}_{ref}, \hat{\beta}_{ref}\right). \tag{33}$$

Substituting $\partial \hat{H}/\partial \hat{R}_{ref} = \sin\hat{\beta}_{ref}$ and $\partial \hat{H}/\partial \hat{\beta}_{ref} = \hat{R}_{ref}\cos\hat{\beta}_{ref}$ into (33) yields

$$\sigma^2_{\hat{H}} = \left(\sin\hat{\beta}_{ref} \sigma_{\hat{R}_{ref}} \right)^2 + \left(\hat{R}_{ref}\cos\hat{\beta}_{ref} \sigma_{\hat{\beta}_{ref}} \right)^2 + 2\hat{R}_{ref}\sin\hat{\beta}_{ref}\cos\hat{\beta}_{ref} \mathrm{Cov}\left(\hat{R}_{ref}, \hat{\beta}_{ref}\right). \tag{34}$$

Since $\mathrm{Cov}\left(\hat{R}_{ref}, \hat{\beta}_{ref}\right)$ can be positive or negative depending on the signs of the gradients, neglecting it may either underestimate or overestimate the altitude error. Therefore, the complete form (34) is used in the accuracy analysis.

If $\mathrm{Cov}\left(\hat{R}_{ref}, \hat{\beta}_{ref}\right)$ is not taken into account, the altitude estimation error is expressed as follows:

$$\sigma_{\hat{H}} = \sqrt{\left(\frac{\partial \hat{H}}{\partial \hat{R}_{ref}}\sigma_{\hat{R}_{ref}}\right)^2 + \left(\frac{\partial \hat{H}}{\partial \hat{\beta}_{ref}}\sigma_{\hat{\beta}_{ref}}\right)^2} = \sqrt{\left(\sin\hat{\beta}_{ref}\cdot\sigma_{\hat{R}_{ref}}\right)^2 + \left(\hat{R}_{ref}\cos\hat{\beta}_{ref}\cdot\sigma_{\hat{\beta}_{ref}}\right)^2}. \quad (35)$$

3. Aircraft Altitude Estimation Based on Multi-Beams

The adaptive aircraft altitude estimation based on the pitch sum with difference channels achieves a high slant range accuracy but yields a relatively poor grazing angle estimation. Conversely, calculating the grazing angle from inertial navigation and servo information often yields a low accuracy. To mitigate the large grazing angle errors, this study proposes an adaptive aircraft altitude estimation method based on multi-beam modes. This method exploits the varying grazing angles of multi-beams to establish a plurality of equations, thereby eliminating the grazing angle error. Depending on the data acquisition method, this approach is divided into sequential multi-beams and cyclic multi-beams. The multi-beam-based altitude estimation methods are described in detail below.

3.1. Principle and Process

3.1.1. Sequential Multi-Beams

Here, a four-beam mode is used as an example to illustrate the adaptive altitude estimation based on the sequential multi-beams approach. Figure 3 shows the geometry of the sequential four-beam mode. The radar illuminates the same area from four different positions during the flight and receives the echoes, forming four beam positions with different grazing angles. Therefore, four equations can be formulated based on the geometric relationships among the aircraft altitude, slant range, and grazing angle.

$$\begin{cases} H_1 = R_1\sin\left(\beta_1 - \Delta_{\beta_1}\right) \\ H_1 + h_{21} = R_2\sin\left(\beta_1 + \delta_{21} - \Delta_{\beta_1}\right) \\ H_1 + h_{31} = R_3\sin\left(\beta_1 + \delta_{31} - \Delta_{\beta_1}\right) \\ H_1 + h_{41} = R_4\sin\left(\beta_1 + \delta_{41} - \Delta_{\beta_1}\right) \end{cases}. \quad (36)$$

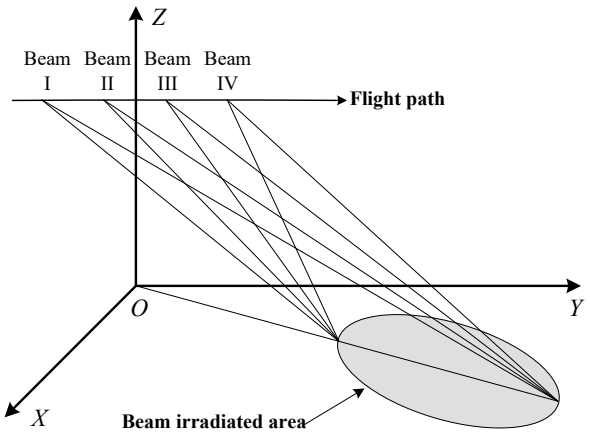


Figure 3. Geometric model of the sequential four-beam mode.

In (36), H_1 stands for the aircraft altitude of beam I, and h_{i1} expresses the relative altitude difference between beam i and beam I. R_i is the slant range of beam i, β_1 is the

grazing angle of beam I, Δ_{β_1} is the error in β_1, and δ_{i1} is the relative grazing-angle difference between beam i and beam I. In (36), h_{i1} is given by inertial information, and R_i is estimated based on the radar echoes. The parameters β_1 and δ_{i1} can either be calculated from INS and servo information or estimated using the pitch sum and difference channel data. The only unknown parameters are H_1 and Δ_{β_1}. Thus, the two parameters can be estimated by solving the equations.

Although H_1, β_1, h_{i1}, and δ_{i1} can be obtained from INS and servo information, the error accumulation of the INS makes the absolute measurement errors of aircraft altitude and attitude angles relatively large. This results in significant errors in H_1 and β_1. In the multi-beam mode, the shorter time intervals between beam positions improve the measurement accuracy of the variations in aircraft altitude and grazing angle. Therefore, both h_{i1} and δ_{i1} are more accurate. In other words, while the absolute measurement error of the INS is larger, its relative error over a short time is small. This characteristic provides the foundation for estimating aircraft altitude in the multi-beam mode.

To quantify the effect of INS relative-error accumulation, the time interval between beam i and beam I is denoted by $T_i = t_i - t_1$. The relative altitude and grazing-angle errors provided by the INS are modeled as functions of T_i. Two commonly used models are considered: a linear drift model and a random-walk model.

For the linear drift model, the relative errors are given by

$$\varepsilon_{h_{i1}}(T_i) = \varepsilon_{h0} + k_h T_i, \quad \varepsilon_{\delta_{i1}}(T_i) = \varepsilon_{\delta 0} + k_\delta T_i, \tag{37}$$

where ε_{h0} and $\varepsilon_{\delta 0}$ are the residual errors at $T_i = 0$ (determined by the short-term INS accuracy and time synchronization error), and k_h, k_δ are the drift rates. For a typical navigation-grade INS, k_h is on the order of $0.1 \sim 1$ m/s and k_δ is on the order of $10^{-4} \sim 10^{-3}\frac{^\circ}{\mathrm{s}}$.

For random-walk model, if the dominant error is random walk, the standard deviations are

$$\sigma_{h_{i1}}(T_i) = \sqrt{\sigma_{h0}^2 + \alpha_h T_i}, \ \sigma_{\delta_{i1}}(T_i) = \sqrt{\sigma_{\delta 0}^2 + \alpha_\delta T_i}, \tag{38}$$

where α_h and α_δ are the random-walk coefficients.

Both models indicate that the relative INS error increases with the beam time interval. For the sequential multi-beam mode, T_i is determined by the platform velocity and the beam spacing:

$$T_i \approx \frac{\Delta R_i}{V}, \tag{39}$$

where ΔR_i is the along-track separation between beam i and beam I, and V is the platform velocity. Therefore, a larger beam spacing improves the geometric sensitivity but increases T_i and, hence, the INS relative error. This is the fundamental trade-off in the sequential multi-beams design.

To solve (36), taking into account that Δ_{β_1} is generally smaller, the equations are expanded using a first-order Taylor series with respect to Δ_{β_1}, yielding a linear system of equations:

$$\begin{cases} H_1 \approx R_1 \sin(\beta_1) - R_1 \cos(\beta_1) \cdot \Delta_{\beta_1} \\ H_1 + h_{21} \approx R_2 \sin(\beta_1 + \delta_{21}) - R_2 \cos(\beta_1 + \delta_{21}) \cdot \Delta_{\beta_1} \\ H_1 + h_{31} \approx R_3 \sin(\beta_1 + \delta_{31}) - R_3 \cos(\beta_1 + \delta_{31}) \cdot \Delta_{\beta_1} \\ H_1 + h_{41} \approx R_4 \sin(\beta_1 + \delta_{41}) - R_4 \cos(\beta_1 + \delta_{41}) \cdot \Delta_{\beta_1} \end{cases}. \tag{40}$$

The system is then rearranged and expressed in matrix form:

$$\mathbf{AX} = \mathbf{Y}. \tag{41}$$

where

$$\mathbf{A} = \begin{bmatrix} 1 & R_1\cos(\beta_1) \\ 1 & R_2\cos(\beta_1+\delta_{21}) \\ 1 & R_3\cos(\beta_1+\delta_{31}) \\ 1 & R_4\cos(\beta_1+\delta_{41}) \end{bmatrix}, \mathbf{X} = \begin{bmatrix} H_1 \\ \Delta_{\beta_1} \end{bmatrix}, \mathbf{Y} = \begin{bmatrix} R_1\sin(\beta_1) \\ R_2\sin(\beta_1+\delta_{21}) - h_{21} \\ R_3\sin(\beta_1+\delta_{31}) - h_{31} \\ R_4\sin(\beta_1+\delta_{41}) - h_{41} \end{bmatrix}. \tag{42}$$

Based on the least squares criterion, the solution to the system is given by the following:

$$\hat{\mathbf{X}} = \left(\mathbf{A}^{\mathbf{T}}\mathbf{A}\right)^{-1}\mathbf{A}^{\mathbf{T}}\mathbf{Y}. \tag{43}$$

Rewriting the matrix equation in scalar form, the estimated aircraft altitude is obtained as follows:

$$\hat{H}_1 = \frac{C_{(Rc\beta)2}\cdot C_{Rs\beta-h} - C_{Rc\beta}\cdot C_{(Rc\beta)(Rs\beta-h)}}{4C_{(Rc\beta)2} - C_{Rc\beta}^2}, \tag{44}$$

where

$$\begin{aligned} C_{Rc\beta} &= \textstyle\sum_{i=1}^{4} R_i\cos(\beta_1+\delta_{i1}), \\ C_{(Rc\beta)2} &= \textstyle\sum_{i=1}^{4}[R_i\cos(\beta_1+\delta_{i1})]^2, \\ C_{Rs\beta-h} &= \textstyle\sum_{i=1}^{4}[R_i\sin(\beta_1+\delta_{i1}) - h_{i1}], \\ C_{(Rc\beta)(Rs\beta-h)} &= \textstyle\sum_{i=1}^{4}[R_i\cos(\beta_1+\delta_{i1})][R_i\sin(\beta_1+\delta_{i1}) - h_{i1}]. \end{aligned} \tag{45}$$

In the above formula, $\delta_{11} = 0, h_{11} = 0$.

The sequential four-beam altitude estimation mode derived above neglects the effect of the Earth's curvature, assuming the geometric relationship between beam I and beam i shown in Figure 4. However, in practice, due to the high aircraft altitude and the long operating range of the radar, the effect of Earth's curvature on the multi-beam mode must be considered.

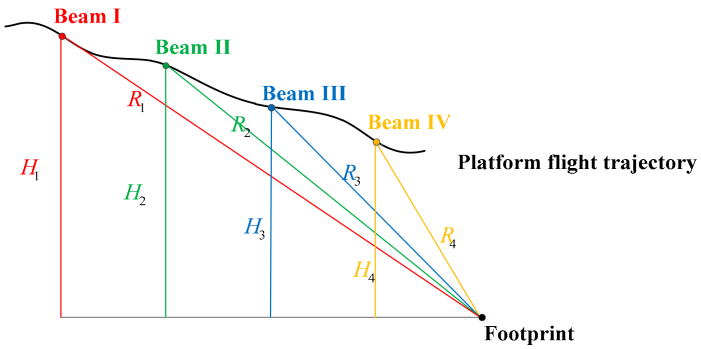


Figure 4. Sequential four-beam mode without considering the effect of Earth's curvature.

Figure 5 illustrates the geometric relationship between beam I and beam i considering the Earth's curvature. In this figure, the position of beam i is translated to align vertically with beam I; thus, their ground illumination points are no longer coincident. Here, H_1 denotes the altitude of beam I, which is the parameter to be estimated. The quantities h_{f1} and h_{fi} represent the ellipsoidal heights (relative to the Earth's datum) of beam I and beam i, respectively, while h_{fi1} is the differential ellipsoidal height between beam i and beam I. The terms h_{g1} and h_{gi} denote the ellipsoidal heights at the ground footprints of beam I and beam i, respectively. For sequential multi-beam operation in spotlight mode, these two values are equal. The Earth is approximated as a sphere with radius R_E over the region between the platform and the illuminated area. The quantity h_{gi1} represents the differential ellipsoidal height of the ground footprint of beam i projected onto the platform altitude direction, relative to that of beam I. This $h_{fi1} - h_{gi1}$ is equivalent to h_{i1} in (36). The ellipsoidal height for each beam, h_{fi}, is provided by the INS. Although the INS has significant absolute errors,

the differential ellipsoidal height between beams, h_{fi1}, achieves relatively high accuracy. The ellipsoidal heights of the ground footprints are predetermined during the experimental design. Based on the geometry shown in Figure 5, the expression for h_{gi1} can be derived as follows:

$$\begin{aligned} h_{gi1}\left(\Delta_{\beta_1}\right) &= \sqrt{\left(h_{gi}+R_E\right)^2 - R_i^2\cos^2\left(\beta_1+\delta_{i1}-\Delta_{\beta_1}\right)} \\ &\quad -\sqrt{\left(h_{g1}+R_E\right)^2 - R_i^2\cos^2\left(\beta_1-\Delta_{\beta_1}\right)} \end{aligned}. \tag{46}$$

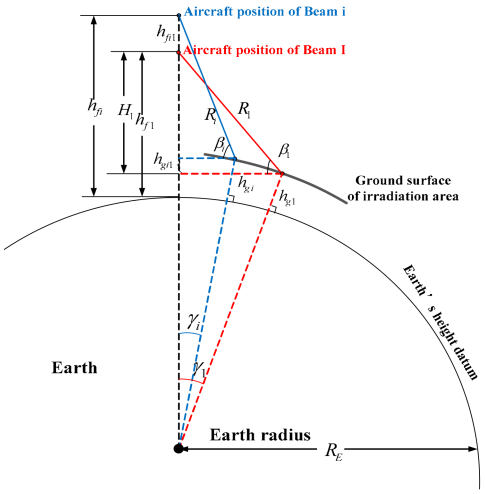


Figure 5. Sequential four-beams mode with considering the effect of Earth's curvature.

Then, the geometric relationship among the platform altitude, beam-center slant range, and grazing angle can be formulated as the following system of equations:

$$\begin{cases} H_1 = R_1\sin\left(\beta_1-\Delta_{\beta_1}\right) \\ H_1+h_{f21} = R_2\sin\left(\beta_1+\delta_{21}-\Delta_{\beta_1}\right)+h_{g21}\left(\Delta_{\beta_1}\right) \\ H_1+h_{f31} = R_3\sin\left(\beta_1+\delta_{31}-\Delta_{\beta_1}\right)+h_{g31}\left(\Delta_{\beta_1}\right) \\ H_1+h_{f41} = R_4\sin\left(\beta_1+\delta_{41}-\Delta_{\beta_1}\right)+h_{g41}\left(\Delta_{\beta_1}\right) \end{cases}. \tag{47}$$

Similarly, applying a first-order Taylor series expansion to each equation in (47) with respect to Δ_{β_1} yields the following linear system:

$$\begin{cases} H_1 \approx R_1\sin(\beta_1) - R_1\cos(\beta_1)\Delta_{\beta_1} \\ H_1+h_{f21} \approx \left[R_2\sin(\beta_1+\delta_{21})+h_{g21}^{(0)}\right] - \left[R_2\cos(\beta_1+\delta_{21})-h_{g21}^{(1)}\right]\Delta_{\beta_1} \\ H_1+h_{f31} \approx \left[R_3\sin(\beta_1+\delta_{31})+h_{g31}^{(0)}\right] - \left[R_3\cos(\beta_1+\delta_{31})-h_{g31}^{(1)}\right]\Delta_{\beta_1} \\ H_1+h_{f41} \approx \left[R_4\sin(\beta_1+\delta_{41})+h_{g41}^{(0)}\right] - \left[R_4\cos(\beta_1+\delta_{41})-h_{g41}^{(1)}\right]\Delta_{\beta_1} \end{cases}, \tag{48}$$

where

$$\begin{aligned} h_{gi1}^{(0)} &= \sqrt{\left(h_{gi}+R_E\right)^2 - R_i^2\cos^2(\beta_1+\delta_{i1})} - \sqrt{\left(h_{g1}+R_E\right)^2 - R_1^2\cos^2(\beta_1)}, \\ h_{gi1}^{(1)} &= \frac{-R_i^2\cos(\beta_1+\delta_{i1})\sin(\beta_1+\delta_{i1})}{\sqrt{\left(h_{gi}+R_E\right)^2-R_i^2\cos^2(\beta_1+\delta_{i1})}} + \frac{-R_1^2\cos(\beta_1)\sin(\beta_1)}{\sqrt{\left(h_{g1}+R_E\right)^2-R_1^2\cos^2(\beta_1)}}. \end{aligned} \tag{49}$$

This linear system can be expressed in matrix form as follows:

$$\mathbf{BM} = \mathbf{N}, \tag{50}$$

where

$$\mathbf{B} = \begin{bmatrix} 1 & R_1\cos(\beta_1) \\ 1 & R_2\cos(\beta_1+\delta_{21}) - h_{g21}^{(1)} \\ 1 & R_3\cos(\beta_1+\delta_{31}) - h_{g31}^{(1)} \\ 1 & R_4\cos(\beta_1+\delta_{41}) - h_{g41}^{(1)} \end{bmatrix}, \quad \mathbf{M} = \begin{bmatrix} H_1 \\ \Delta_{\beta_1} \end{bmatrix},$$
$$\mathbf{N} = \begin{bmatrix} R_1\sin(\beta_1) \\ R_2\sin(\beta_1+\delta_{21}) + h_{g21}^{(0)} - h_{f21} \\ R_3\sin(\beta_1+\delta_{31}) + h_{g31}^{(0)} - h_{f31} \\ R_4\sin(\beta_1+\delta_{41}) + h_{g41}^{(0)} - h_{f41} \end{bmatrix}. \tag{51}$$

Based on the least-squares criterion, the numerical solution to the system is obtained as follows:

$$\hat{\mathbf{M}} = \left(\mathbf{B}^{\mathrm{T}}\mathbf{B}\right)^{-1}\mathbf{B}^{\mathrm{T}}\mathbf{N}. \tag{52}$$

The estimated platform altitude is then given as follows:

$$\hat{H}_1 = \frac{D_{(Rc\beta)2}\cdot D_{Rs\beta-h} - D_{Rc\beta}\cdot D_{(Rc\beta)(Rs\beta-h)}}{4D_{(Rc\beta)2} - {D_{Rc\beta}}^2}, \tag{53}$$

where

$$\begin{gathered} D_{Rc\beta} = \sum_{j=1}^{4}\left[R_i\cos(\beta_1+\delta_{i1}) - h_{gi1}^{(1)}\right] \quad D_{(Rc\beta)2} = \sum_{j=1}^{4}[R_i\cos(\beta_1+\delta_{i1}) - h_{gi1}^{(1)}]^2 \\ D_{Rs\beta-h} = \sum_{j=1}^{4}\left[R_i\sin(\beta_1+\delta_{i1}) + h_{gi1}^{(0)} - h_{fi1}\right] \\ D_{(Rc\beta)(Rs\beta-h)} = \sum_{j=1}^{4}\left[R_i\cos(\beta_1+\delta_{i1}) - h_{gi1}^{(1)}\right]\left[R_i\sin(\beta_1+\delta_{i1}) + h_{gi1}^{(o)} - h_{fi1}\right] \end{gathered} \tag{54}$$

In the above formula, $\delta_{11} = 0$, $h_{f11} = 0$, $h_{g11}^{(0)} = 0$, $h_{g11}^{(1)} = 0$.

The ground-footprint height h_{g1} in (46) is a prior parameter. In practice, it is obtained from a digital elevation model, a map, or an assumed reference plane, and therefore contains an error δh_g. To evaluate how this prior error propagates to the altitude estimate, a sensitivity analysis is performed.

The sensitivity of the Earth-curvature correction term $h_{gi1}\left(\Delta_{\beta_1}\right)$ to h_{g1} is derived. Differentiating (46) with respect to h_{g1} yields

$$\frac{\partial h_{gi1}}{\partial h_{g1}} = \frac{h_{g1}+R_E}{\sqrt{\left(h_{g1}+R_E\right)^2 - R_i^2\cos^2\left(\beta_1+\delta_{i1}-\Delta_{\beta_1}\right)}} - \frac{h_{g1}+R_E}{\sqrt{\left(h_{g1}+R_E\right)^2 - R_i^2\cos^2\left(\beta_1-\Delta_{\beta_1}\right)}}. \tag{55}$$

Since $R_E \gg R_i$ and $h_{g1} \ll R_E$, each square-root term can be approximated as

$$\sqrt{\left(h_{g1}+R_E\right)^2 - R_i^2\cos^2(\cdot)} \approx \left(h_{g1}+R_E\right)\left[1 - \frac{R_i^2\cos^2(\cdot)}{2\left(h_{g1}+R_E\right)^2}\right], \tag{56}$$

and therefore

$$\frac{\partial h_{gi1}}{\partial h_{g1}} \approx \frac{R_i^2}{2\left(h_{g1}+R_E\right)^2}\left[\cos^2\left(\beta_1-\Delta_{\beta_1}\right) - \cos^2\left(\beta_1+\delta_{i1}-\Delta_{\beta_1}\right)\right]. \tag{57}$$

Because $R_i/\left(h_{g1}+R_E\right) \sim 10^{-3}$, the sensitivity in (57) is on the order of 10^{-6}, i.e., a 10 m error in h_{g1} changes h_{gi1} by only about 10^{-5} m. This means that, for the sequential multi-beam mode, where all beams illuminate the same footprint and h_{g1} is the common reference, the prior error δh_g is largely canceled in the differential term h_{gi1}. The residual altitude bias is

$$\left|\delta H_1^{(h_g,\mathrm{seq})}\right| \approx \left|\sum_{i=2}^{4}\frac{\partial h_{gi1}}{\partial h_{g1}}\right|\cdot\left|\delta h_g\right| \ll \left|\delta h_g\right|. \tag{58}$$

3.1.2. Cyclic Multi-Beams

Since the sequential multi-beam mode forms multiple illumination beams sequentially at intervals during platform movement, it requires a relatively long data acquisition time. For SAR platforms with highly maneuverable trajectories, this mode is impractical for real-time altitude estimation. Furthermore, it is difficult to guarantee a common grazing-angle error across all beams. To address this issue, an aircraft altitude estimation method based on the cyclic multi-beam mode is proposed. In this mode, a servo system controls the antenna to rapidly illuminate different areas of the imaging scene within a short time, forming multiple beams with different grazing angles.

The principle of the cyclic multi-beam-based altitude estimation method is introduced using a four-beam example. Figure 6 illustrates the geometric model of this method, where CPI denotes the coherent processing interval. The solid rectangle represents the SAR imaging scene, and the dashed rectangle is the circumscribed boundary. During flight, the servo system directs the beam to illuminate the four different vertices of this circumscribed rectangle sequentially within a short time. The formulation and solution of the geometric equations for this mode are identical to those of the sequential four-beam case. For the cyclic four-beam mode, the effect of Earth's curvature also be considered, and the geometric relationship between beam I and beam i is the same as that shown in Figure 5. Since different beams illuminate different areas, the ellipsoidal heights at their ground footprints also differ.

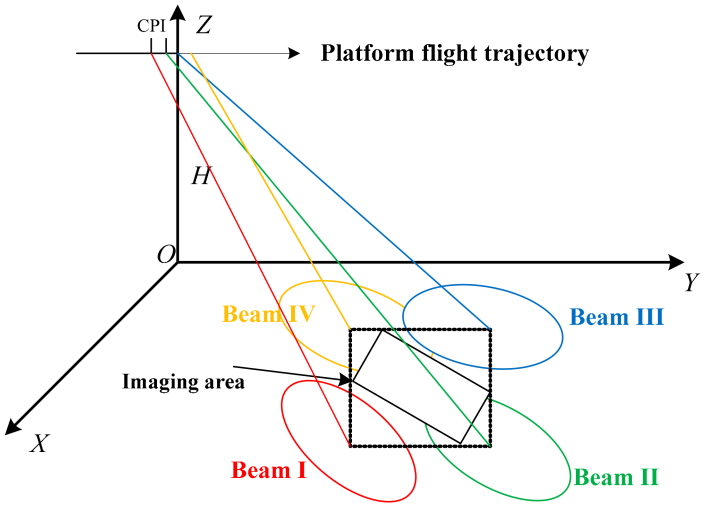


Figure 6. Cyclic four-beam mode without considering the effect of Earth's curvature.

Because the beams of the cyclic mode illuminate different patches, the mean scattering coefficients of these patches may differ. However, the angle measurement in this work is based on the ratio of the difference-channel and sum-channel data, i.e.,

$$\frac{d_{i,n}}{s_{i,n}} = \frac{\sum_m \sigma_{i,m} A_\Delta(\xi_{i,m}) e^{j\phi_m}}{\sum_m \sigma_{i,m} A_\sum(\xi_{i,m}) e^{j\phi_m}}, \tag{59}$$

where $\sigma_{i,m}$ is the scattering coefficient of the mth scatterer in the nth range cell of beam i. If the mean scattering coefficient of the patch is denoted by $\overline{\sigma}_i$ and the local variation around the mean is denoted by $\delta\sigma_{i,m} = \sigma_{i,m} - \overline{\sigma}_i$, the ratio becomes

$$\frac{d_{i,n}}{s_{i,n}} = \frac{\overline{\sigma}_i \sum_m A_\Delta(\xi_{i,m}) e^{j\phi_m} + \sum_m \delta\sigma_{i,m} A_\Delta(\xi_{i,m}) e^{j\phi_m}}{\overline{\sigma}_i \sum_m A_\sum(\xi_{i,m}) e^{j\phi_m} + \sum_m \delta\sigma_{i,m} A_\sum(\xi_{i,m}) e^{j\phi_m}}. \tag{60}$$

When the within-patch scattering is approximately uniform, i.e., $\delta\sigma_{i,m} \approx 0$, the mean scattering coefficient $\overline{\sigma}_i$ appears as a common factor in both the numerator and the denominator and is canceled:

$$\frac{d_{i,n}}{s_{i,n}} \approx \frac{\sum_m \mathrm{A}_\Delta(\xi_{i,m})e^{j\phi_m}}{\sum_m A_\Sigma(\xi_{i,m})e^{j\phi_m}}. \tag{61}$$

Therefore, the patch-to-patch difference in the mean scattering coefficient does not directly bias the angle estimate of an individual beam. This is because the angle information is carried by the ratio of the two channel responses, in which the common amplitude factor is canceled. Consequently, the zero-depth position of the angle curve, which determines the beam-center slant range R_i, is not shifted by the patch-to-patch scattering difference.

The scattering difference still affects the angle measurement in an indirect way: the mean scattering coefficient determines the SNR of each beam,

$$\mathrm{SNR}_i = \frac{E_{s,i}}{E_{n,i}}. \tag{62}$$

The angle measurement variance is approximately inversely proportional to SNR_i. A weaker-scattering patch, therefore, has a larger angle measurement variance. This effect changes the precision of the angle estimate, but not its mean. In the multi-beam solution, this is handled by the weighted least squares described below.

The residual within-patch scattering non-uniformity, i.e., the $\delta\sigma_{i,m}$ term in (60), may produce a small angle bias if it is correlated with the local angle. This term is much smaller than the mean scattering difference, and it is suppressed by the per-beam angle-bias correction in (14), by excluding range cells with abrupt scattering changes, and by multi-look averaging over homogeneous patches.

Because the patch-to-patch scattering difference changes the SNR and, hence, the angle measurement variance of each beam, the cyclic multi-beams equations are solved by weighted least squares:

$$\hat{\mathbf{M}}_W = \left(\mathbf{B^T W B}\right)^{-1}\mathbf{B^T W N}, \quad \mathbf{W} = \mathrm{diag}(\omega_1, \ldots, \omega_M), \tag{63}$$

where $\omega_i \propto SNR_i$. This weight reduces the influence of weak-scattering patches on the altitude estimate. When all patches have the same scattering coefficient, ω_i is equal for all beams and (63) reduces to the equal-weight solution.

For the cyclic multi-beam mode, the beam switching time is much shorter, typically on the order of milliseconds to tens of milliseconds, so the time interval T_i is small and the INS relative error is close to ε_{h0} and $\varepsilon_{\delta 0}$. This is one of the advantages of the cyclic mode over the sequential mode in terms of INS error accumulation. However, different beams illuminate different patches, and the ground-footprint elevations h_{g1}, h_{g2}, h_{g3}, and h_{g4} are independent. In this case, the elevation difference $h_{gi1} = h_{gi} - h_{g1}$ has an error $\delta h_{gi1} = \delta h_{gi} - \delta h_{g1}$. To the first order, this error propagates directly to the altitude estimate:

$$\left|\delta H_1^{(h_g,\mathrm{cyc})}\right| \approx \frac{1}{M}\sum_{i=2}^{4}\left(\delta h_{gi} - \delta h_{g1}\right), \tag{64}$$

where M is the number of beams. If the patch elevation errors are independent and have the same standard deviation σ_{h_g}, the standard deviation of the altitude bias is

$$\sigma H_1^{(h_g,\mathrm{cyc})} \approx \sqrt{\frac{2(M-1)}{M^2}}\sigma_{h_g}. \tag{65}$$

For $M = 4$, this coefficient is $\sqrt{6/16} \approx 0.61$; i.e., the altitude bias is about $0.61\sigma_{h_g}$. This is much larger than the sequential case in (58). Therefore, the cyclic multi-beam mode is more sensitive to the prior ground-footprint elevation error, and a more accurate digital elevation model or a local elevation reference is required for this mode.

3.2. Estimation Accuracy

3.2.1. System Approximation Error

Here, we analyze the error introduced by the approximation from (47) to (48). If the approximation is not applied and the higher-order terms of the Taylor series are retained, the system is expressed as follows:

$$\begin{cases} H_1 = R_1\sin(\beta_1) - R_1\cos(\beta_1)\Delta_{\beta_1} + O_1\left(\Delta_{\beta_1}\right) \\ H_1 + h_{f21} = \left[R_2\sin(\beta_1+\delta_{21}) + h_{g21}^{(0)}\right] - \left[R_2\cos(\beta_1+\delta_{21}) - h_{g21}^{(1)}\right]\Delta_{\beta_1} + O_2\left(\Delta_{\beta_1}\right) \\ H_1 + h_{f31} = \left[R_3\sin(\beta_1+\delta_{31}) + h_{g31}^{(0)}\right] - \left[R_3\cos(\beta_1+\delta_{31}) - h_{g31}^{(1)}\right]\Delta_{\beta_1} + O_3\left(\Delta_{\beta_1}\right) \\ H_1 + h_{f41} = \left[R_4\sin(\beta_1+\delta_{41}) + h_{g41}^{(0)}\right] - \left[R_4\cos(\beta_1+\delta_{41}) - h_{g41}^{(1)}\right]\Delta_{\beta_1} + O_4\left(\Delta_{\beta_1}\right) \end{cases} \tag{66}$$

where $O_i\left(\Delta_{\beta_1}\right)$ represents the higher-order terms of the Taylor expansion, given by

$$\begin{aligned} O_i\left(\Delta_{\beta_1}\right) &= \beta_i\sin\left(\beta_1+\delta_{i1}-\Delta_{\beta_1}\right) - \left[R_i\sin(\beta_1+\delta_{i1}) - R_i\cos(\beta_1+\delta_{i1})\Delta_{\beta_1}\right] \\ &= \left[-\tfrac{1}{2}R_i\sin(\beta_1+\delta_{i1}) + h_{gi1}^{(2)}\right]\Delta_{\beta_1}^2 + \left[\tfrac{1}{6}R_i\cos\left(\beta_1+\delta_{i1}\right) + h_{gi1}^{(3)}\right]\Delta_{\beta_1}^3 + \cdots . \end{aligned} \tag{67}$$

To theoretically analyze how the approximation error varies with the common grazing angle error Δ_{β_1}, the higher-order term $O_i\left(\Delta_{\beta_1}\right)$ is bounded. For clarity, the Earth-curvature correction terms $h_{gi1}^{k}(k \geq 2)$ are small compared with the leading terms and are neglected in the bound analysis; their contribution is included in the numerical verification below.

Starting from the definition of $O_i\left(\Delta_{\beta_1}\right)$ in (67) and using the trigonometric identity,

$$\sin\left(\beta_i - \Delta_{\beta_1}\right) = \sin\beta_i\cos\Delta_{\beta_1} - \cos\beta_i\sin\Delta_{\beta_1}, \tag{68}$$

with $\beta_i \triangleq \beta_1 + \delta_{i1}$, the higher-order term can be rewritten as

$$O_i\left(\Delta_{\beta_1}\right) = R_i\left[\sin\beta_i\left(\cos\Delta_{\beta_1} - 1\right) + \cos\beta_i\left(\Delta_{\beta_1} - \sin\Delta_{\beta_1}\right)\right]. \tag{69}$$

Using the standard inequalities,

$$\left|\cos\Delta_{\beta_1} - 1\right| \leq \frac{\Delta_{\beta_1}^2}{2}, \quad \left|\Delta_{\beta_1} - \sin\Delta_{\beta_1}\right| \leq \frac{\Delta_{\beta_1}^3}{6}, \quad \Delta_{\beta_1} \geq 0\,. \tag{70}$$

The magnitude of $O_i\left(\Delta_{\beta_1}\right)$ is bounded by

$$\left|O_i\left(\Delta_{\beta_1}\right)\right| \leq R_i\left(\frac{\Delta_{\beta_1}^2}{2} + \frac{\Delta_{\beta_1}^3}{6}\right). \tag{71}$$

Equation (71) shows that the leading term of the approximation error is $O_i\left(\Delta_{\beta_1}^2\right)$; i.e., the error grows quadratically with the common grazing angle error. The cubic term $O_i\left(\Delta_{\beta_1}^3\right)$ becomes non-negligible only when Δ_{β_1} is large. More precisely, the relative contribution of the cubic term to the bound is $\Delta_{\beta_1}/3$, so the quadratic bound is dominant when $\Delta_{\beta_1} \ll 3$ rad, which is always satisfied in practical SAR geometry.

If the Earth-curvature correction terms are retained, the bound becomes

$$\left|O_i\left(\Delta_{\beta_1}\right)\right| \leq R_i\left(\frac{\Delta_{\beta_1}^2}{2} + \frac{\Delta_{\beta_1}^3}{6}\right) + \left|h_{gi1}^{(2)}\right|\Delta_{\beta_1}^2 + \left|h_{gi1}^{(3)}\right|\Delta_{\beta_1}^3, \tag{72}$$

where $h_{gi1}^{(2)}$ and $h_{gi1}^{(3)}$ are the second- and third-order Earth-curvature correction coefficients in (67). Since $h_{gi1}^{(2)}$ and $h_{gi1}^{(3)}$ are on the order of meters and Δ_{β_1} is on the order of 10^{-2}rad, their contributions are much smaller than the leading $R_i\Delta_{\beta_1}^2/2$ term. Therefore, the $O_i\left(\Delta_{\beta_1}^2\right)$ growth law remains valid.

Define the dimensionless approximation error ratio as follows:

$$\eta_i\left(\Delta_{\beta_1}\right) \triangleq \frac{O_i\left(\Delta_{\beta_1}\right)}{R_i} \leq \frac{\Delta_{\beta_1}^2}{2} + \frac{\Delta_{\beta_1}^3}{6}. \tag{73}$$

Equation (73) provides a geometry-independent upper bound on the relative approximation error of each equation. It will be used in (78)–(80) to bound the relative error of the least-squares solution.

Thus, (66) can be expressed as follows:

$$\mathbf{BM} = \mathbf{N} + \mathbf{Z}. \tag{74}$$

Here, **B**, **M**, and **N** are the same as those in (50), and **Z** represents the error term caused by the approximation:

$$\mathbf{Z} = \left[O_1\left(\Delta_{\beta_1}\right) \quad O_2\left(\Delta_{\beta_1}\right) \quad O_3\left(\Delta_{\beta_1}\right) \quad O_4\left(\Delta_{\beta_1}\right)\right]^{\mathrm{T}}. \tag{75}$$

Applying the least squares criterion to (74) yields

$$\hat{\mathbf{M}}_{\mathbf{accu}} = \left(\mathbf{B}^{\mathrm{T}}\mathbf{B}\right)^{-1}\mathbf{B}^{\mathrm{T}}(\mathbf{N} + \mathbf{Z}) = \hat{\mathbf{M}} + \left(\mathbf{B}^{\mathrm{T}}\mathbf{B}\right)^{-1}\mathbf{B}^{\mathrm{T}}\mathbf{Z}. \tag{76}$$

Comparing $\hat{\mathbf{M}}_{\mathbf{accu}}$ with $\hat{\mathbf{M}}$ in (52), the difference lies in the second term containing **Z.** Therefore, the approximation of the system is given by

$$\hat{\delta}_{\hat{\mathbf{M}}} = \left(\mathbf{B}^{\mathbf{T}}\mathbf{B}\right)^{-1}\mathbf{B}^{\mathbf{T}}\mathbf{Z}. \tag{77}$$

Combining (71) and (77), the norm of the approximation-induced error is bounded by

$$\left\|\hat{\delta}_{\hat{\mathbf{M}}}\right\| \leq \left\|\left(\mathbf{B}^{\mathbf{T}}\mathbf{B}\right)^{-1}\mathbf{B}^{\mathbf{T}}\right\| \cdot \|\mathbf{Z}\| . \tag{78}$$

Using (71) and the fact that $\|\mathbf{Z}\| \leq \sqrt{M}\max_i|O_i|$, where M is the number of beams, we obtain

$$\|\mathbf{Z}\| \leq \sqrt{M}R_{\max}\left(\frac{\Delta_{\beta_1}^2}{2} + \frac{\Delta_{\beta_1}^3}{6}\right), \tag{79}$$

where $R_{\max} = \max_i R_i$. Therefore, the relative approximation error of the estimated parameter vector satisfies

$$\frac{\left\|\hat{\delta}_{\hat{\mathbf{M}}}\right\|}{\left\|\hat{\mathbf{M}}\right\|} \leq \kappa(\mathbf{B}) \cdot \frac{\|\mathbf{Z}\|}{\|\mathbf{N}\|} \leq C_B\left(\frac{\Delta_{\beta_1}^2}{2} + \frac{\Delta_{\beta_1}^3}{6}\right), \tag{80}$$

where $\kappa(\mathbf{B}) = \|\mathbf{B}\|\left\|\left(\mathbf{B}^{\mathbf{T}}\mathbf{B}\right)^{-1}\mathbf{B}^{\mathbf{T}}\right\|$ is the condition number of the observation matrix, and $C_B = \kappa(\mathbf{B})\sqrt{M}R_{\max}/\|\mathbf{N}\|$ is a constant independent of Δ_{β_1} for a given beam geometry.

Equation (80) establishes the theoretical variation law of the approximation error: the relative error of the multi-beam least-squares solution grows quadratically with the common grazing angle error Δ_{β_1}, with a cubic correction term. This provides a rigorous justification for the first-order Taylor approximation: as long as Δ_{β_1} is small enough that $C_B\Delta_{\beta_1}^2/2$ is below the required accuracy, the approximation error can be neglected.

The magnitude of the model approximation error is evaluated through numerical calculations. Tables 1 and 2 list the typical geometric parameters for the sequential and cyclic four-beams modes, respectively, considering Earth's curvature. A common grazing angle error of $\Delta_{\beta_1} = 1^{\circ}$ among the beams and the Earth radius of approximately 6371 km are assumed. Tables 3 and 4 present the corresponding model approximation errors for these two modes. It is evident from the tables that the quantity **Z** is extremely small relative to the term **N**. Consequently, the difference between $\hat{\mathbf{M}}$ and $\hat{\mathbf{M}}_{\mathbf{accu}}$ is negligible. The approximation

error of the system, $\hat{\delta}_{\hat{\mathbf{M}}}$, is only 0.015% of $\hat{\mathbf{M}}_{\mathbf{accu}}$, which indicates that this error can be safely neglected. Therefore, for multi-beam modes, it is reasonable to approximate the nonlinear geometric equations using a first-order Taylor series expansion. For the sequential four-beam geometry in Table 1 and the cyclic four-beam geometry in Table 2, the constant C_B can be numerically evaluated. Using the parameters in these tables, $C_B \approx 0.015$ for the sequential mode and $C_B \approx 0.013$ for the cyclic mode. Therefore, when $\Delta_{\beta_1} = 1^\circ \approx 0.01745$ rad, the relative approximation error is bounded by $0.015 \times \left(0.01745^2/2\right) \approx 2.3 \times 10^{-6}$, which is consistent with the numerical result 0.015% in Table 3. For the cyclic mode, the relative approximation error is also of the same order of magnitude as that of the sequential mode. This agreement validates the theoretical bound (80).

Table 1. Geometric parameters of the sequential four-beam mode.

Beam Number	I	II	III	IV
Aircraft altitude H_i (m)	4000	3990	3980	3950
Slant range R_i (km)	15	13	11	9
Grazing angle β_i (°)	15.47	17.87	21.21	26.03
Beam ellipsoidal height h_{fi} (m)	4983.60	4977.99	4971.75	4944.87
Inter-beam ellipsoidal height variation h_{fi1} (m)	0	−5.61	−11.85	−38.73
Footprint ellipsoidal height h_{gi} (km)	1	1	1	1
Ellipsoidal height variation at the projected footprint point h_{gi1} (m)	0	4.39	8.15	11.27

Table 2. Geometric parameters of the cyclic four-beam mode.

Beam Number	I	II	III	IV
Aircraft altitude H_i (m)	4000	3998	3996	3994
Slant range R_i (km)	11	13.7	13.2	10.3
Grazing angle β_i (°)	21.3	17.0	17.6	22.8
Beam ellipsoidal height h_{fi} (m)	4991.76	4984.53	4983.58	4986.93
Inter-beam ellipsoidal height variation h_{fi1} (m)	0	−7.23	−8.18	−4.83
Footprint ellipsoidal height h_{gi} (km)	1	1	1	1
Ellipsoidal height variation at the projected footprint point h_{gi1} (m)	0	−5.23	−4.18	1.17

Table 3. Approximation error results for the sequential four-beam mode.

N	Z	$\hat{\mathbf{M}}$	$\hat{\mathbf{M}}_{\mathbf{accu}}$	$\hat{\boldsymbol{\delta}}_{\hat{\mathbf{M}}}$
$\begin{bmatrix} 4251.70 \\ 4215.30 \\ 4178.31 \\ 4140.46 \end{bmatrix}$	$\begin{bmatrix} -0.6348 \\ -0.6309 \\ -0.6268 \\ -0.6193 \end{bmatrix}$	$\begin{bmatrix} 4000.60 \\ 0.017456 \end{bmatrix}$	$\begin{bmatrix} 4000.00 \\ 0.017453 \end{bmatrix}$	$\begin{bmatrix} -0.6011 \\ -2.39 \times 10^{-6} \end{bmatrix}$

Table 4. Approximation error results for the cyclic four-beam mode.

N	Z	$\hat{\mathbf{M}}$	$\hat{\mathbf{M}}_{\mathbf{accu}}$	$\hat{\boldsymbol{\delta}}_{\hat{\mathbf{M}}}$
$\begin{bmatrix}4178.22\\4228.11\\4218.98\\4165.08\end{bmatrix}$	$\begin{bmatrix}-0.6273\\-0.6305\\-0.6296\\-0.6255\end{bmatrix}$	$\begin{bmatrix}4000.61\\0.017455\end{bmatrix}$	$\begin{bmatrix}4000.00\\0.017453\end{bmatrix}$	$\begin{bmatrix}-0.6138\\-1.28\times10^{-6}\end{bmatrix}$

3.2.2. Aircraft Altitude Accuracy

Since $h_{fi1}-h_{gi1}$ is equivalent to h_{i1} in (36), only h_{i1} is considered as the altitude variation error source to simplify the analysis, while h_{fi1} and h_{gi1} are not treated separately. After approximating the system of equations, the adaptive multi-beams altitude estimation results are mainly affected by three error sources:

- The beam-center slant range error R_i, determined by locating the zero-depth position of the difference channel;
- The grazing angle variation error δ_{i1} between beam positions, calculated from inertia navigation and attitude information;
- The aircraft altitude variation error h_{i1} between beam positions, provided by the inertial navigation information.

Based on the principle of error propagation, the altitude estimation error is expressed as follows:

$$\varepsilon_{H_1}=\sqrt{\sum_{i=1}^{4}\left(\frac{\partial\hat{H}_1}{\partial R_i}\varepsilon_{R_i}\right)^2+\sum_{i=2}^{4}\left(\frac{\partial\hat{H}_1}{\partial\delta_{i1}}\varepsilon_{\delta_{i1}}\right)^2+\sum_{i=2}^{4}\left(\frac{\partial\hat{H}_1}{\partial h_{i1}}\varepsilon_{h_{i1}}\right)^2}\,, \tag{81}$$

where ε_{R_i}, $\varepsilon_{\delta_{i1}}$, and $\varepsilon_{h_{i1}}$ are the errors of R_i, δ_{i1}, and h_{i1}, respectively. According to (44), the partial derivatives are given by

$$\begin{aligned}\frac{\partial\hat{H}_1}{\partial\overline{\omega}}=&-\frac{\left(C_{(Rc\beta)2}\cdot C_{Rs\beta-h}-C_{Rc\beta}\cdot C_{(Rc\beta)(Rs\beta-h)}\right)}{\left(4C_{(Rc\beta)2}-C_{Rc\beta}^2\right)^2}\left(4\frac{\partial C_{(Rc\beta)2}}{\partial\overline{\omega}}-2C_{Rc\beta}\frac{\partial C_{Rc\beta}}{\partial\overline{\omega}}\right)\\&+\frac{C_{Rs\beta-h}\cdot\frac{\partial C_{(Rc\beta)2}}{\partial\overline{\omega}}+C_{(Rc\beta)2}\cdot\frac{\partial C_{Rs\beta-h}}{\partial\overline{\omega}}-C_{(Rc\beta)(Rs\beta-h)}\cdot\frac{\partial C_{Rc\beta}}{\partial\overline{\omega}}-C_{Rc\beta}\cdot\frac{\partial C_{(Rc\beta)(Rs\beta-h)}}{\partial\overline{\omega}}}{4C_{(Rc\beta)2}-C_{Rc\beta}^2}.\end{aligned} \tag{82}$$

Here, $\overline{\omega}$ represents any of the variables R_i, δ_{i1}, or h_{i1}. The partial derivative expressions are as follows:

$$\begin{aligned}&\frac{\partial C_{Rc\beta}}{\partial R_i}=\cos(\beta_1+\delta_{i1})\,,\quad\frac{\partial C_{Rs\beta-h}}{\partial R_i}=\sin(\beta_1+\delta_{i1}),\frac{\partial C_{(Rc\beta)2}}{\partial R_i}=2R_i\cos^2(\beta_1+\delta_{i1})\,,\\&\frac{\partial C_{(Rc\beta)(Rs\beta-h)}}{\partial R_i}=2R_i\cos(\beta_1+\delta_{i1})\sin(\beta_1+\delta_{i1})-h_{i1}\cos(\beta_1+\delta_{i1}),\end{aligned} \tag{83}$$

$$\frac{\partial C_{Rc\beta}}{\partial h_{i1}}=0,\quad\frac{\partial C_{Rs\beta-h}}{\partial h_{i1}}=-1,\frac{\partial C_{(Rc\beta)2}}{\partial h_{i1}}=0\,,\quad\frac{\partial C_{(Rc\beta)(Rs\beta-h)}}{\partial h_{i1}}=-R_i\cos(\beta_1+\delta_{i1}), \tag{84}$$

$$\begin{aligned}&\frac{\partial C_{Rc\beta}}{\partial\delta_{i1}}=-R_i\sin(\beta_1+\delta_{i1})\,,\quad\frac{\partial C_{Rs\beta-h}}{\partial\delta_{i1}}=R_i\cos(\beta_1+\delta_{i1}),\\&\frac{\partial C_{(Rc\beta)2}}{\partial\delta_{i1}}=-2R_i^2\cos(\beta_1+\delta_{i1})\sin(\beta_1+\delta_{i1})\,,\\&\frac{\partial C_{(Rc\beta)(Rs\beta-h)}}{\partial\delta_{i1}}=R_i^2\left[2\cos^2(\beta_1+\delta_{i1})-1\right]+h_{i1}R_i\sin(\beta_1+\delta_{i1}).\end{aligned} \tag{85}$$

It should be noted that the approximation error $\hat{\delta}_{\hat{\mathbf{M}}}$ analyzed in Section 3.2.1 is a systematic bias caused by the first-order Taylor truncation, while the three error sources above are random errors in the observations. They are independent and should be treated separately. From (71) and (80), the approximation-induced altitude bias is bounded by

$$\left|\delta H_1^{\text{approx}}\right|\le\kappa(\mathbf{B})\sqrt{M}R_{\max}\left(\frac{\Delta_{\beta_1}^2}{2}+\frac{\Delta_{\beta_1}^3}{6}\right)\cdot\|\hat{\mathbf{M}}\|. \tag{86}$$

For the typical geometry in Table 1 and $\Delta_{\beta_1} = 1°$, this bias is on the order of 10^{-2} m, which is much smaller and can be neglected. However, when Δ_{β_1} exceeds a few degrees, the approximation bias should be added to the statistical error budget:

$$\varepsilon_{H_1}^{\text{total}} = \sqrt{\varepsilon_{H_1}^2 + \left(\delta H_1^{\text{approx}}\right)^2}, \tag{87}$$

where ε_{H_1} is given by (81). For the present simulation and measured data, the approximation bias is negligible compared with ε_{H_1}.

In addition to the statistical error in (81) and the Taylor-approximation bias in (86), the prior ground-footprint elevation error δh_g also introduces an altitude bias. According to the sensitivity analysis in (58)–(65), the bias is mode-dependent:

$$\delta H_1^{(h_g)} = \begin{cases} \sum_{i=2}^{M} \dfrac{\delta h_{gi1}}{\delta h_{g1}} \delta h_g \,, & \text{sequential mode,} \\ \dfrac{1}{M} \sum_{i=2}^{M} \left(\delta h_{gi} - \delta h_{g1}\right), & \text{cyclic mode.} \end{cases} \tag{88}$$

For the sequential mode, the coefficient in (58) is on the order of 10^{-6}, so the bias is negligible even for a 10 m prior error. For the cyclic mode, assuming independent patch elevation errors with standard deviation σ_{h_g}, the bias standard deviation is given by (65). Therefore, the total altitude error including all three sources is

$$\varepsilon_{H_1}^{\text{total}} = \sqrt{\varepsilon_{H_1}^2 + \left(\delta H_1^{\text{approx}}\right)^2 + \left(\delta H_1^{(h_g)}\right)^2}, \tag{89}$$

where the three terms correspond to the random statistical error, the Taylor-approximation bias, and the ground-footprint elevation prior bias, respectively. For the sequential mode, the third term is negligible; for the cyclic mode, it should be included when σ_{h_g} is not much smaller than the required altitude accuracy.

The statistical error ε_{H_1} in (81) depends on the INS relative errors $\varepsilon_{\delta_{i1}}$ and $\varepsilon_{h_{i1}}$. Substituting the time-dependent models (37) or (38) into (81) yields

$$\varepsilon_{H_1}(T) = \sqrt{\sum_{i=1}^{M} \left(\frac{\partial \hat{H}_1}{\partial R_i} \varepsilon_{R_i}\right)^2 + \sum_{i=2}^{M} \left(\frac{\partial \hat{H}_1}{\partial \delta_{i1}} \varepsilon_{\delta_{i1}}(T_i)\right)^2 + \sum_{i=2}^{M} \left(\frac{\partial \hat{H}_1}{\partial h_{i1}} \varepsilon_{h_{i1}}(T_i)\right)^2}, \tag{90}$$

where $T_i = t_i - t_1$ is the time interval between beam i and beam I. For the sequential mode, $T_i \approx \Delta R_i / V$; for the cyclic mode, T_i is the beam switching time and is much smaller.

To quantify the degradation caused by INS relative-error accumulation, define the degradation factor as

$$\gamma_H(T) \triangleq \frac{\varepsilon_{H_1}(T)}{\varepsilon_{H_1}(0)}, \tag{91}$$

where $\varepsilon_{H_1}(0)$ is the altitude error at $T = 0$, i.e., when the INS relative error is at its short-term level. Using (37), (90) becomes

$$\varepsilon_{H_1}(T) = \sqrt{\sum_{i=1}^{M} \left(\frac{\partial \hat{H}_1}{\partial R_i} \varepsilon_{R_i}\right)^2 + \sum_{i=2}^{M} \left(\frac{\partial \hat{H}_1}{\partial \delta_{i1}} (\varepsilon_{\delta 0} + k_\delta T_i)\right)^2 + \sum_{i=2}^{M} \left(\frac{\partial \hat{H}_1}{\partial h_{i1}} (\varepsilon_{h0} + k_h T_i)\right)^2}. \tag{92}$$

Equation (92) shows that the altitude error grows approximately linearly with T when the INS drift terms dominate, and the growth rate is determined by k_h, k_δ, and the partial derivatives $\partial \hat{H}_1 / \partial h_{i1}$, $\partial \hat{H}_1 / \partial \delta_{i1}$.

The total altitude error including all sources is

$$\varepsilon_{H_1}^{\text{total}}(T) = \sqrt{\varepsilon_{H_1}^2(T) + \left(\delta H_1^{\text{approx}}\right)^2 + \left(\delta H_1^{(h_g)}\right)^2}. \tag{93}$$

The multi-beam altitude estimation relies on the relative grazing-angle variation δ_{i1} and the relative altitude variation h_{i1} provided by the INS. In the nominal case, these errors are $\varepsilon_{\delta 0}$ and ε_{h0}. To evaluate the limit performance of the method, the INS relative errors are gradually increased beyond the nominal values:

$$\varepsilon_{\delta_{i1}} = \kappa_\delta \varepsilon_{\delta_0}, \quad \varepsilon_{h_{i1}} = \kappa_h \varepsilon_{h_0}, \tag{94}$$

where $\kappa_\delta \geq 1$ and $\kappa_h \geq 1$ are degradation factors. Substituting (94) into (90) yields the altitude error under degraded INS relative measurements:

$$\varepsilon_{H_1}(\kappa_\delta, \kappa_h) = \sqrt{\sum_{i=1}^{M} \left(\frac{\partial \hat{H}_1}{\partial R_i} \varepsilon_{R_i}\right)^2 + \sum_{i=2}^{M} \left(\frac{\partial \hat{H}_1}{\partial \delta_{i1}} \kappa_\delta \varepsilon_{\delta_0}\right)^2 + \sum_{i=2}^{M} \left(\frac{\partial \hat{H}_1}{\partial h_{i1}} \kappa_h \varepsilon_{h_0}\right)^2}, \tag{95}$$

Define the failure threshold as

$$\varepsilon_{H_1}(\kappa_\delta, \kappa_h) = \sigma_H^{\text{req}}, \tag{96}$$

where σ_H^{req} is the required altitude accuracy, e.g., 10 m or 1% of the true altitude. The solution of (96) defines the allowable degradation boundary $\left(\kappa_\delta^{\max}, \kappa_h^{\max}\right)$ of the INS relative measurements. If $\kappa_\delta > \kappa_\delta^{\max}$ or $\kappa_h > \kappa_h^{\max}$, the multi-beam method can no longer meet the required altitude accuracy.

Because the partial derivatives $\partial \hat{H}_1 / \partial \delta_{i1}$ and $\partial \hat{H}_1 / \partial h_{i1}$ are determined by the beam geometry, the allowable degradation boundary is mode-dependent. For the sequential mode, the beam spacing is large and the geometry is more sensitive, but the time interval is long and the INS errors are larger. For the cyclic mode, the beam switching time is short, so the nominal INS relative errors are smaller, but the geometry may be less diverse.

The estimation accuracy of the multi-beam-based aircraft altitude estimation method is evaluated through numerical calculations. The typical geometric parameters for the sequential and cyclic four-beam modes (given in Tables 1 and 2, respectively) are adopted for the analysis. A common grazing angle error Δ_{β_1} of 1° among beams is assumed. The error sources for the sequential and cyclic four-beam modes are listed in Tables 5 and 6, respectively. Monte Carlo simulations are performed to obtain the statistical altitude estimation errors, which are then compared with the theoretical results calculated using (81). The estimation error results for the two multi-beam methods are presented in Tables 7 and 8, respectively. Four simulation cases are considered: three cases where only one error source is active, and one case where all three error sources are present simultaneously. The tables show that the theoretical and numerical results are in close agreement, validating (81).

Table 5. Error sources for aircraft altitude estimation in the sequential four-beam mode.

Error Source	Slant Range R_i (m)	Variation in Grazing Angle δ_{i1} (°)	Variation in Aircraft Altitude h_{i1} (m)
3σ error	20	0.05	10

Table 6. Error sources for aircraft altitude estimation in the cyclic four-beam mode.

Error Source	Slant Range R_i (m)	Variation in Grazing Angle δ_{i1} (°)	Variation in Aircraft Altitude h_{i1} (m)
3σ error	20	0.02	5

Table 7. Altitude estimation errors under different combinations of error sources in the sequential four-beam mode.

	Slant Range Error	Variation in Grazing Angle Error	Variation in Aircraft Altitude Error	Aircraft Altitude Estimation 3σ Error (m)	
				Theoretical Calculation	Numerical Simulation
Simulation I	√	-	-	18.73	18.66
Simulation II	-	√	-	22.65	22.50
Simulation III	-	-	√	20.31	20.23
Simulation IV	√	√	√	35.72	35.78

Note: "√" indicates the presence of the corresponding error source in the simulation, whereas "-" indicates its absence.

Table 8. Altitude estimation errors under different combinations of error sources in the cyclic four-beam mode.

	Slant Range Error	Variation in Grazing Angle Error	Variation in Aircraft Altitude Error	Aircraft Altitude Estimation 3σ Error (m)	
				Theoretical Calculation	Numerical Simulation
Simulation I	√	-	-	26.54	26.45
Simulation II	-	√	-	14.47	14.33
Simulation III	-	-	√	17.02	16.89
Simulation IV	√	√	√	34.69	34.59

Note: "√" indicates the presence of the corresponding error source in the simulation, whereas "-" indicates its absence.

3.3. Computational Complexity

The computational complexity of the proposed algorithms based on the pitch sum with difference channels and multi-beams is analyzed respectively.

3.3.1. Aircraft Altitude Estimation Method Based on Pitch Sum with Difference Channels

For a single altitude estimation using the pitch sum with difference channels, the number of range points is N_r and the number of azimuth points is N_a.

Step I: Measuring the pitch angle from the pitch sum with difference channel echoes. Each complex multiplication requires six floating-point operations. Since each complex division contains two complex multiplications, it requires 12 floating-point operations. According to (5), the complex divisions in this step require $12N_rN_a$ floating-point operations. After obtaining the pitch angle sequence for each PRT, the pitch angles of the same range cells are averaged. This averaging process requires N_rN_a operations. Thus, the computational complexity of this step is given by

$$S_{I,I} = 13N_rN_a\,. \tag{97}$$

Step II: Estimating the quadratic curve coefficients $\hat{a}$, $\hat{b}$, and $\hat{c}$. In (20), the dimensions of matrix $\mathbf{R}$ and matrix $\mathbf{R}^{\mathbf{T}}\mathbf{R}$ are $N_r \times 3$ and 3×3, respectively. Since N_r is on the order of thousands, the computational complexity of (20) is dominated by the matrix multiplication. In contrast, the computational complexity of inverting the 3×3 square matrix $\mathbf{R}^{\mathbf{T}}\mathbf{R}$ is negligible. The floating-point operations for multiplying matrix $\mathbf{A}_1$ (dimensions $P_1 \times P_2$)

by matrix $\mathbf{A}_2$ (dimensions $P_2 \times P_3$) are $2p_1p_2p_3$. Thus, the computational complexity of this step is given by

$$S_{I,II} = 42N_r \, . \tag{98}$$

Step III: Estimating the beam-center slant range and grazing angle, and calculating the aircraft altitude. Compared with the first two steps, the computational complexities of (7), (10), (11), and (12) are negligible.

Therefore, the computational complexity of the whole algorithm based on the pitch sum with difference channels is given by

$$S_{I,com} = S_{I,I} + S_{I,II} = 13N_rN_a + 42N_r \, . \tag{99}$$

3.3.2. Aircraft Altitude Estimation Method Based on Multi-Beams

For a single altitude estimation using the multi-beams, the number of beams is M. For each beam, the numbers of range and azimuth points are N_r and N_a, respectively.

Step I: Estimating the beam-center slant ranges of the multi-beams. Based on the complexity analysis of the first algorithm, the complexity of this step is given by

$$S_{II,I} = M(13N_rN_a + 42N_r). \tag{100}$$

Step II: Estimating the aircraft altitude. In (52), the dimensions of matrix $\mathbf{B}$ and matrix $\mathbf{B^TB}$ are $M \times 2$ and 2×2, respectively. The computational complexity of inverting the 2×2 square matrix $\mathbf{B^TB}$ is negligible. Thus, this step is dominated by the matrix multiplication and is given by

$$S_{II,II} = 18M \, . \tag{101}$$

Therefore, the computational complexity of the whole multi-beam algorithm is given by

$$S_{II,com} = S_{II,I} + S_{II,II} = M(13N_rN_a + 42N_r + 18). \tag{102}$$

The floating-point operation counts in (97)–(102) can be converted into an estimated processing time. Let P denote the effective floating-point performance of the target hardware (in FLOP/s), and η the computational efficiency (ratio of achieved to peak performance). The estimated processing time is

$$T_{\text{proc}} \approx \frac{S_{\text{com}}}{P_\eta}, \tag{103}$$

where S_{com} is the total floating-point operation count from (99) or (102). Equation (103) provides a theoretical estimate of the processing time; it is not a hardware measurement. The actual processing time depends on the instruction-level parallelism, memory access, and implementation details, and will be measured on an embedded airborne processor in future work.

The above expression indicates that the computational complexity of the multi-beam algorithm increases considerably as the number of beams grows.

3.4. Beam Position Design Criteria

In least-squares estimation, a larger number of observations under the same error conditions generally lead to more accurate parameter estimates. For multi-beam altitude estimation, increasing the number of beams improves measurement accuracy. However, it also significantly increases the computational complexity of solving the system of equations (due to larger matrix dimensions). This degrades real-time performance. Therefore, in practical applications, the number of beams must be selected as a trade-off between the required altitude accuracy and real-time processing capability. For the multi-beam algorithm, the beam spacing can be designed based on the required altitude estimation. Here,

a four-beam mode is used as an example, discussed in terms of the sequential and cyclic multi-beams, respectively.

3.4.1. Sequential Four-Beams

For analysis purposes, it is assumed that the altitudes of the four beams and the slant range of beam I are as given in Table 1. The differences in slant ranges, ΔR, between adjacent beams are equal. The common grazing angle error among the beams Δ_{β_1} is 1°. The error sources are listed in Table 5. Based on (81), the relationship between the aircraft altitude estimation error and ΔR is calculated and plotted in Figure 7a. It can be seen that as ΔR increases, the beam spacing becomes larger, which significantly improves the altitude measurement accuracy. On the other hand, since the four beams are formed sequentially during the platform flight, a larger beam spacing requires a longer acquisition time. In practice, the beam spacing should be increased as much as possible to improve accuracy, provided that the real-time constraints and accuracy requirements are both satisfied. If the time required to form the sequential four beams fails to meet the real-time requirement while maintaining the desired altitude accuracy, the cyclic four-beams method should be adopted instead.

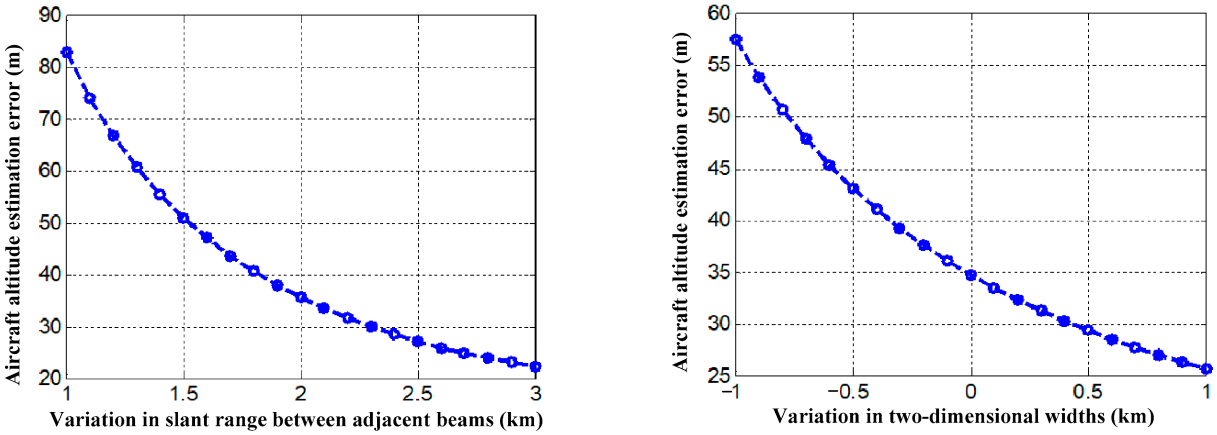


Figure 7. Beam interval design criteria for the multi-beam algorithm. (**a**) Aircraft altitude estimation error versus ΔR. (**b**) Aircraft altitude estimation error versus ΔW.

The above discussion considered only the geometric sensitivity. When the INS relative-error accumulation is taken into account, the altitude error as a function of ΔR becomes

$$\varepsilon_{H_1}(\Delta R) = \sqrt{\begin{array}{c}\sum_{i=1}^{M}\left(\frac{\partial \hat{H}_1}{\partial R_i}\varepsilon_{R_i}\right)^2 + \sum_{i=2}^{M}\left(\frac{\partial \hat{H}_1}{\partial \delta_{i1}}\left(\varepsilon_{\delta 0} + k_\delta \frac{(i-1)\Delta R}{V}\right)\right)^2 \\ + \sum_{i=2}^{M}\left(\frac{\partial \hat{H}_1}{\partial h_{i1}}\left(\varepsilon_{h0} + k_h \frac{(i-1)\Delta R}{V}\right)\right)^2\end{array}}. \quad (104)$$

Equation (104) shows that $\varepsilon_{H_1}(\Delta R)$ is the sum of two competing effects: the geometric term $\sum_{i=1}^{M}\left(\frac{\partial \hat{H}_1}{\partial R_i}\varepsilon_{R_i}\right)^2$ decreases with increasing ΔR (because the beam geometry becomes more diverse), while the INS terms increase with ΔR (because the time interval grows). Therefore, there exists an optimal beam spacing ΔR_{opt} that minimizes the total altitude error:

$$\Delta R_{\text{opt}} = \arg\min_{\Delta R} \varepsilon_{H_1}(\Delta R). \quad (105)$$

The optimal spacing can be found numerically from (104). For the parameters in Table 1 and typical navigation-grade INS drift rates, ΔR_{opt} is on the order of a few kilometers. This

provides a quantitative design criterion for the sequential multi-beam mode: the beam spacing should be chosen around ΔR_{opt} to balance the geometric sensitivity and the INS relative-error accumulation.

To obtain a closed-form relation between the beam spacing ΔR and the altitude accuracy, the linearized equations in (40) are written in the following form:

$$H_1 + h_{i1} = R_i \sin(\beta_1 + \delta_{i1}) - c_i\,\Delta_{\beta_1}, \quad c_i = R_i \cos(\beta_1 + \delta_{i1}), \tag{106}$$

where $i = 1, \ldots, M$ and $h_{11} = 0$, $\delta_{11} = 0$. In matrix form, $\mathbf{AX} = \mathbf{Y}$ with $\mathbf{A} = [1, \mathbf{c}]$, $\mathbf{X} = \left[H_1, \Delta_{\beta_1}\right]^{\mathbf{T}}$, and $\mathbf{c} = [c_1, \ldots, c_M]^{\mathrm{T}}$. The least-squares covariance of $\hat{H}_1$ is

$$\sigma_{H_1}^2 = \left[\left(\mathbf{A}^{\mathrm{T}}\mathbf{C}_Y^{-1}\mathbf{A}\right)^{-1}\right]_{11}, \tag{107}$$

where $\mathbf{C}_Y$ is the covariance matrix of the observation errors. For simplicity, assume equal observation accuracy $\mathbf{C}_Y = \sigma_Y^2\mathbf{I}$. Then,

$$\sigma_{H_1}^2 = \sigma_Y^2\left[\frac{1}{M} + \frac{\bar{c}^2}{\sum_{i=1}^{M}(c_i - \bar{c})^2}\right], \tag{108}$$

where $\bar{c} = \frac{1}{M}\sum_{i=1}^{M} c_i$. For the sequential mode with equal beam spacing ΔR, the slant range of beam i is approximately $R_i \approx R_1 - (i-1)\Delta R$, and the corresponding c_i changes approximately linearly with ΔR. Using the derivative $dc/dR = 1/\cos\beta$ derived from $H = R\sin\beta$, the spacing of c_i is

$$\Delta c \approx \frac{\Delta R}{\cos\beta}. \tag{109}$$

For M equally spaced beams, $\sum_{i=1}^{M}(c_i - \bar{c})^2 = \Delta c^2 M\left(M^2 - 1\right)/12$. Substituting into (108) yields

$$\sigma_{H_1,\mathrm{geo}}^2 = \sigma_Y^2\left[\frac{1}{M} + \frac{12\bar{c}^2}{\Delta c^2 M(M^2-1)}\right] = \sigma_Y^2\left[\frac{1}{M} + \frac{12\bar{c}^2\cos^2\beta}{\Delta R^2 M(M^2-1)}\right]. \tag{110}$$

Equation (110) is the analytical design formula for the sequential mode. For $M = 4$, it becomes

$$\sigma_{H_1,\mathrm{geo}}^2 = \sigma_Y^2\left[\frac{1}{4} + \frac{\bar{c}^2\cos^2\beta}{5\Delta R^2}\right]. \tag{111}$$

When the beam spacing is large enough that the second term dominates, (111) reduces to

$$\sigma_{H_1,\mathrm{geo}} \approx \frac{\sigma_Y\,\bar{c}\cos\beta}{\sqrt{5}\Delta R}, \tag{112}$$

i.e., the geometric altitude accuracy is inversely proportional to the beam spacing ΔR. This is the quantitative form of the trend observed in Figure 7a.

When the INS relative-error accumulation is included, the total altitude error is obtained by replacing σ_Y in (110) with the beam-dependent observation errors. According to (104), the total error is

$$\sigma_{H_1,\mathrm{total}}^2 = \sigma_{H_1,\mathrm{geo}}^2(\Delta R) + \sum_{i=2}^{M}\left(\frac{\partial\hat{H}_1}{\partial\delta_{i1}}(\varepsilon_{\delta 0} + k_\delta T_i)\right)^2 + \sum_{i=2}^{M}\left(\frac{\partial\hat{H}_1}{\partial h_{i1}}(\varepsilon_{h0} + k_h T_i)\right)^2, \tag{113}$$

Combining (110) and (113), the required beam spacing for a given accuracy requirement σ_H^{req} can be obtained by solving

$$\sigma_{H_1,\mathrm{total}}(\Delta R) = \sigma_H^{\mathrm{req}} \tag{114}$$

numerically for ΔR. Equation (114) is the inverse design formula that can be directly used to determine the required beam spacing without running simulations.

If the INS relative-error accumulation is negligible (e.g., for short beam intervals or high-grade INS), (111) can be inverted directly:

$$\Delta R_{\text{req}} = \frac{\bar{c}\cos\beta}{\sqrt{\left(\sigma_H^{\text{req}}/\sigma_Y\right)^2 - 1/M}\ \sqrt{M(M^2-1)/12}}. \tag{115}$$

For $M = 4$, this becomes

$$\Delta R_{\text{req}} = \frac{\bar{c}\cos\beta}{\sqrt{5\left[\left(\sigma_H^{\text{req}}/\sigma_Y\right)^2 - 1/4\right]}}. \tag{116}$$

Equation (116) provides a closed-form design formula: given the required altitude accuracy σ_H^{req}, the observation error σ_Y , and the geometry parameters $\bar{c}$ and β, the required beam spacing ΔR_{req} can be calculated directly.

3.4.2. Cyclic Four Beams

For analysis purposes, the altitudes of the four beams are assumed as given in Table 2. The initial two-dimensional widths are approximately 3 km × 1 km (Range × Azimuth). The center of the imaging area remains fixed. The two-dimensional widths are expanded symmetrically from the original size, and the variations in both dimensions, ΔW, are kept equal. The common grazing angle error among the beams Δ_{β_1} is 1°. The error sources are listed in Table 6. Based on (81), the relationship between the aircraft altitude estimation error and ΔW is calculated and plotted in Figure 7b. It can be seen that, as ΔW increases, the beam spacing becomes larger, significantly improving the altitude measurement accuracy. In practice, the cyclic four-beam mode can be rapidly formed within a short time using beam control, based on the actual size of the imaging area. If the required accuracy is not met, the imaging area size can be increased to improve the altitude estimation accuracy. For the cyclic multi-beam mode, T_i is the beam switching time and is typically much smaller than $\Delta R/V$, so the INS terms are close to $\varepsilon_{\delta 0}$ and ε_{h0}, and the altitude error is dominated by the geometric term and the slant range error. This is a significant advantage of the cyclic mode for real-time operation.

In the cyclic mode, the beam spacing is determined by the size of the imaging area. Let ΔW denote the change in the two-dimensional width of the imaging area. The corresponding change in the grazing angle is

$$\delta\beta_i \approx \frac{\partial\beta}{\partial W}\Delta W, \tag{117}$$

where $\partial\beta/\partial W$ is determined by the geometry of the imaging area and the platform altitude. For a rectangular imaging area with width W at slant range R and altitude H, the grazing angle is approximately $\beta \approx \arcsin(H/R)$, and

$$\frac{\partial\beta}{\partial W} \approx \frac{\partial\beta}{\partial R}\frac{\partial R}{\partial W} = -\frac{H}{R^2\cos\beta}\cdot\frac{\partial R}{\partial W}. \tag{118}$$

For a side-looking geometry, $\partial R/\partial W \approx \cos\beta$, so

$$\frac{\partial\beta}{\partial W} \approx -\frac{H}{R^2} = -\frac{\sin\beta}{R}. \tag{119}$$

The corresponding change in $c_i = R_i\cos\beta_i$ is

$$\Delta c_i \approx -R_i\sin\beta_i\delta\beta_i \approx R_i\sin\beta_i\frac{\sin\beta_i}{R_i}\Delta W = \sin^2\beta_i\Delta W. \tag{120}$$

Substituting (120) into (110) yields the geometric altitude error of the cyclic mode,

$$\sigma_{H_1,\mathrm{geo}}^2 = \sigma_Y^2\left[\frac{1}{M} + \frac{12\bar{c}^2}{\Delta W^2 \sin^4\beta\, M(M^2-1)}\right]. \tag{121}$$

For $M = 4$, this becomes

$$\sigma_{H_1,\mathrm{geo}}^2 = \sigma_Y^2\left[\frac{1}{4} + \frac{\bar{c}^2}{5\Delta W^2 \sin^4\beta}\right]. \tag{122}$$

When the second term dominates, the geometric altitude accuracy is inversely proportional to $\Delta W \sin^2\beta$:

$$\sigma_{H_1,\mathrm{geo}} \approx \frac{\sigma_Y\,\bar{c}}{\sqrt{5}\Delta W \sin^2\beta}. \tag{123}$$

The required imaging-area size for a given accuracy requirement is

$$\Delta W_{\mathrm{req}} = \frac{\bar{c}}{\sqrt{5\left[\left(\sigma_H^{\mathrm{req}}/\sigma_Y\right)^2 - 1/4\right]}\sin^2\beta}\,. \tag{124}$$

Equation (124) is the closed-form design formula for the cyclic mode. It shows that the required imaging-area size decreases as the grazing angle increases, because a larger grazing angle produces a larger $dc/d\beta$ and, hence, a larger geometric sensitivity.

Based on (110)–(116) and (121)–(124), the beam-position design procedure can be carried out directly as follows:

For the sequential mode:

1. Calculate the observation error σ_Y from the beam-center slant-range error in (28) and the angle-bias correction in (14);
2. Given the required altitude accuracy σ_H^{req}, use (116) to obtain the initial beam spacing ΔR_{req} when the INS drift is negligible;
3. If the INS drift is not negligible, solve (114) numerically to obtain ΔR_{req}, or use the optimal spacing in (105) as a starting point;
4. Check that the resulting beam spacing satisfies the real-time constraint $T = (M-1)\Delta R/V \le T_{\max}$, where $T_{\max}$ is determined from the estimated total time in Section 3.5 and (129).

For the cyclic mode:

1. Calculate σ_Y as above;
2. Use (124) to obtain the required imaging-area size ΔW_{req};
3. Check that the resulting beam switching time satisfies the real-time constraint.

Because the estimated processing time is small compared with the acquisition time, $T_{\max}$ is mainly determined by the acquisition time and the beam interval/switching time.

The analytical design formulae in (110)–(116) and (121)–(124) assume nominal INS relative errors. When the INS relative index degrades, the design formulae should be modified by replacing $\varepsilon_{\delta 0}$ and ε_{h0} with $\kappa_\delta \varepsilon_{\delta_0}$ and $\kappa_h \varepsilon_{h_0}$. The required beam spacing or imaging-area size then becomes a function of the degradation factors:

$$\Delta R_{\mathrm{req}} = f_R^{-1}\left(\sigma_H^{\mathrm{req}}; \kappa_\delta, \kappa_h\right), \qquad \Delta W_{\mathrm{req}} = f_W^{-1}\left(\sigma_H^{\mathrm{req}}; \kappa_\delta, \kappa_h\right). \tag{125}$$

Equation (125) provides a direct way to check whether a given beam position design remains valid when the INS relative index degrades. If the required spacing exceeds the real-time or geometric constraint, the cyclic mode or a higher-grade INS should be considered.

The above discussion analyzed the beam position design criteria for a fixed number of beams. Alternatively, the altitude estimation accuracy can be adjusted by varying the number of beams. Using the sequential multi-beam mode as an example, with a common grazing angle error Δ_{β_1} of 1° among beams, the geometric parameters are given in Table 9, and the error sources are listed in Table 5. Monte Carlo simulations are performed to obtain the numerical altitude estimation errors, and the theoretical errors are calculated using (81). The results are presented in Table 10. Six simulation cases are designed, corresponding to different numbers of beams and different beam positions, while considering errors in slant range, altitude variation, and grazing angle variation simultaneously. The numerical results show good agreement with the theoretical calculations. Furthermore, the aircraft altitude estimation accuracy improves as the number of beams increases.

Table 9. Geometric parameters of the sequential multi-beam mode.

Beam Number	I	II	III	IV	V
Aircraft altitude H_i (m)	4000	3990	3980	3950	3900
Slant range R_i (km)	15	13	11	9	7
Grazing angle β_i (°)	15.47	17.87	21.21	26.03	33.86

Table 10. Altitude estimation errors for different beam combinations in the sequential multi-beam mode.

Beam Number	I	II	III	IV	V	Aircraft Altitude Estimation 3σ Error (m)	
						Theoretical Calculation	Numerical Simulation
Simulation I	√	√	√	-	-	61.64	61.74
Simulation II	-	√	√	√	-	48.59	48.46
Simulation III	-	-	√	√	√	38.36	38.21
Simulation IV	√	√	√	√	-	35.72	35.78
Simulation V	-	√	√	√	√	28.84	28.70
Simulation VI	√	√	√	√	√	21.34	21.51

Note: "√" indicates the presence of the corresponding error source in the simulation, whereas "-" indicates its absence.

3.5. Estimated Processing Time and Total Time

The computational complexity in Section 3.3 is expressed in floating-point operations. In this subsection, the processing time is estimated from (103) under an assumed hardware platform, and the total time needed to obtain one altitude estimate from all beams is derived. It should be emphasized that the processing time reported here is a theoretical estimate based on the operation count, not a hardware measurement. The actual hardware-in-the-loop processing time will be measured in future work.

Assumed hardware platform: The target platform is a TI TMS320C6678 DSP (8 C66x cores at 1.25 GHz, 320 GFLOPS peak single-precision performance). Because the algorithm is dominated by per-range-cell complex division and small-matrix inversion, the effective performance is taken as $P_{\text{eff}} = 2$ GFLOPS, i.e., about 0.6% of the peak, which is a conservative assumption for DSP-based per-point complex arithmetic.

Estimated processing time: Substituting the operation counts in (99) and (102) into (103), with $N_r = 1024$, $N_a = 64$, and $M = 4$, yields

$$T_{\text{proc,single}} \approx \frac{0.895 \times 10^6}{2 \times 10^9} \approx 0.45 \text{ ms}, \quad T_{\text{proc,multi}} \approx \frac{3.58 \times 10^6}{2 \times 10^9} \approx 1.79 \text{ ms}. \tag{126}$$

Including a factor of two for indexing, loop control, and function-call overhead, the estimated processing times are about 0.9 ms for the single-beam method and 3.6 ms for the four-beam method. These estimates are summarized in Table 11.

Table 11. Estimated processing time for one altitude estimate (theoretical estimate from (103); not a hardware measurement).

Method	S_{com} (MFLOP)	P_{eff} (GFLOP)	Estimated T_{proc} (ms)
Single-beam	0.895	2	0.9
Sequential four-beam	3.58	2	3.6
Cyclic four-beam	3.58	2	3.6

Total time for all beams: The data acquisition time for 64 PRTs is $T_{\text{acq}} = 32$ ms. For the sequential mode, the beams are acquired at different along-track positions with time interval $T = \Delta R/V$, with $\Delta R = 2$ km and $V = 150$ m/s. The total time is

$$T_{\text{total,seq}} = T_{\text{acq}} + (M-1)T + T_{\text{proc}} = 0.0320 + 40 + 0.0036 = 42.0356 \text{ s}. \tag{127}$$

For the cyclic mode, the beams are switched by the servo system with $T_{\text{sw}} = 20$ ms, and

$$T_{\text{total,cyc}} = T_{\text{acq}} + (M-1)T_{\text{sw}} + T_{\text{proc}} = 0.0320 + 0.060 + 0.0036 = 0.0956 \text{ s}. \tag{128}$$

The total times are summarized in Table 12.

Table 12. Estimated total time for one altitude estimate from all beams.

Mode	T_{acq} (ms)	Beam Intervals/ Switching Time (s)	Estimated T_{proc} (ms)	Estimated T_{total} (s)
Sequential four-beam	32	40	3.6	42.0356
Cyclic four-beam	32	0.06	3.6	0.0956

The estimated processing time (about 0.9–3.6 ms) is much smaller than the data acquisition time (32 ms) and the total time. Therefore, the processing itself does not constitute a real-time bottleneck. For the sequential mode, the total time is dominated by the beam interval (tens of seconds); this mode is suitable for applications where the altitude does not change rapidly over the beam-formation time. For the cyclic mode, the total time is about 96 ms, which is close to a typical SAR real-time update interval and is, therefore, more suitable for real-time altitude estimation. The real-time constraint in Section 3.4 is $T = (M-1)\Delta R/V \le T_{\max}$. From (127), the allowable beam interval for a given total-time budget is

$$T \le \frac{T_{\text{req}} - T_{\text{acq}} - T_{\text{proc}}}{\text{M} - 1}. \tag{129}$$

where T_{req} is the required update interval. Equation (129) links the real-time constraint to the beam-position design and to the INS relative-error accumulation analyzed in

Section 3.2.2. Because the estimated T_{proc} is small, the real-time performance is mainly determined by the acquisition time and the beam interval/switching time. The actual hardware-in-the-loop processing time will be measured on the TMS320C6678 platform in future work.

4. Results

4.1. Simulation

4.1.1. Pitch Sum with Difference Channels

To verify the validity and accuracy of the proposed aircraft altitude estimation method, echo simulations are performed. The simulated scene follows a Rayleigh distribution, and the simulation parameters are listed in Table 13. The signal-to-noise ratio in the table is defined as the ratio of the echo energy at the sum-channel beam center to the noise energy after range pulse compression. The antenna pattern shown in Figure 8 is used, with a beam width of approximately 8° and a difference slope is -0.20 deg^{-1}.

Table 13. Simulation parameters for aircraft altitude estimation based on pitch sum with difference channels.

Beam Number	I
Aircraft altitude H (km)	3.994
Slant range R_{ref} (km)	10.306
Platform velocity V (m/s)	150
Number of range cells N_r	1024
Carrier wavelength λ (m)	0.03
Antenna gain G_{gain} (dB)	35
Azimuth beamwidth θ_A ($^{\circ}$)	1
Ground-range resolution P_{gr} (m)	1
Pulse width T_p (μs)	10
System noise factor F_n (dB)	3
Standard noise temperature T_0 (K)	290
System loss L_{Σ} (dB)	4
Average backscattering coefficient σ_0 (dB)	-15
Radar peak transmit power P_t (kW)	0.032, 0.10, 0.32, 1.00
Signal-to-noise SNR (dB)	5, 10, 15, 20

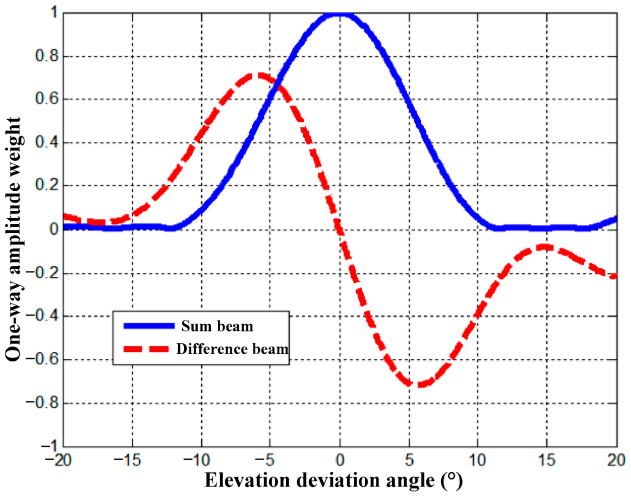


Figure 8. Antenna pattern of pitch sum and difference beams.

According to the radar equation, the SNR at each range cell after range pulse compression is as follows:

$$\mathrm{SNR} = \frac{P_t G_{gain}^2 \sigma_0 \theta_A \rho_{gr} \lambda^2 T_p}{(4\pi)^3 R^3 k T_0 F_n L_\Sigma}, \tag{130}$$

where P_t is the radar peak transmit power, G_{gain} is the antenna gain, σ_0 is the average backscattering coefficient in the radar observation area, θ_A is the antenna azimuth beamwidth, ρ_{gr} is the ground-range resolution, λ is the carrier wavelength, T_p is the pulse width, R is the slant range, k is the Boltzmann constant, T_0 is the standard noise temperature, F_n is the noise factor, and L_Σ is the system loss factor, which includes radome, waveform, and transmission losses.

Here, the angle-bias correction in (14) is verified under an airborne SAR echo simulation. The simulation scene is a Rayleigh-distributed surface, and the following non-ideal factors are included: (i) a channel amplitude inconsistency of 0.5 dB and phase inconsistency of 5°; (ii) scene energy fluctuation; (iii) additive noise; and (iv) a small terrain undulation with $\sigma_h = 2$ m to separate the noise-correction effect from the terrain effect. The SNR is set to 5, 10, 15, and 20 dB by changing the noise level. For each SNR, 1000 Monte Carlo trials are performed, and there is a total of 64,000 pulse repetition time (PRT) echoes. Every 64 PRT echoes are grouped as one dataset for a single aircraft altitude estimation, with a data acquisition time of 32 ms per dataset.

Figure 9 shows the processing results of the first dataset at SNR = 15 dB. Figure 9a,b show the range pulse compression results of the sum and difference channels, respectively. The difference channel result appears as a dark central region; however, the exact zero-depth position is difficult to determine from the amplitude due to noise. Therefore, angle measurement is required. Figure 9c shows the amplitude ratio of the difference and sum channels. Clearly, the near-range region is predominantly negative, while the far-range region is positive. Figure 9d presents the weighted average of the angle measurement from the 64 PRTs. Since the swath is small, the measured angle varies nearly linearly with the slant range. After curve fitting, the beam-center slant range and grazing angle are determined from the fitting coefficients, yielding the estimated aircraft altitude.

The angle bias and the resulting altitude error before and after the correction in (14) are statistically evaluated with the results listed in Table 14. It presents the statistical results of 1000 Monte Carlo sets of data at four SNR levels (5, 10, 15, and 20 dB) to verify the angle-bias correction in (14). The correction significantly improves the angle measurement accuracy, especially at low SNR. Without correction, the grazing angle deviation is highly dependent on the SNR, reaching −5.3974° at 5 dB and −0.4885° at 20 dB. This results in severe altitude estimation errors, with a mean deviation of −894.4769 m at 5 dB. After applying the correction in (14), the mean deviation of β_{ref} stabilizes at approximately −0.27° across all SNR levels. The mean altitude error is significantly reduced to the order of tens of meters, decreasing from −45.0036 m at 5 dB to −43.1188 m at 20 dB.

In addition, the beam-center slant range R_{ref} achieves high accuracy, with errors remaining at the meter level both before and after correction (e.g., mean error of 7.1213 m at 5 dB and 5.0005 m at 20 dB). In contrast, a residual deviation of about 0.27° still exists in the grazing angle estimation after correction. This indicates that, although the zero-crossing location of the angle curve is accurately determined, the error in estimating the slope near the zero-crossing remains significant. According to (35), the remaining altitude estimation error is primarily caused by this residual grazing angle error. Furthermore, the standard deviations of all parameters decrease with increasing SNR, which is consistent with theoretical expectations.

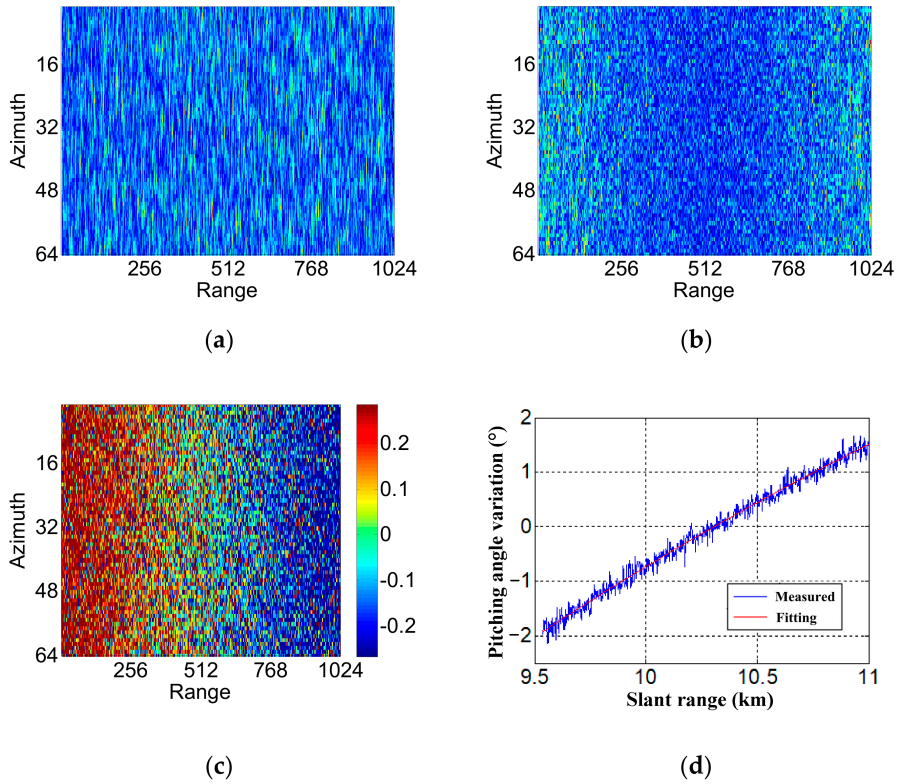


Figure 9. Range pulse compression and angle measurement results for the first dataset of the pitch sum with difference channels at SNR = 15 dB. (**a**) Range pulse compression result of the sum channel. (**b**) Range pulse compression result of the difference channel. (**c**) Amplitude ratio of the difference and sum channels. (**d**) Weighted average angle measurement of multiple PRTs. 'Range' and 'Azimuth' represent the sampling points along the range and azimuth dimensions, respectively.

Table 14. Verification of the angle-bias correction under airborne SAR echo simulation.

SNR (dB)	5	10	15	20
β_{ref} error mean before correction (°)	−5.3974	−2.1798	−0.9168	−0.4885
β_{ref} error std before correction (°)	0.3893	0.2888	0.2147	0.1624
R_{ref} error mean before correction (m)	−7.2325	7.0356	−6.0446	−5.0137
R_{ref} error std before correction (m)	13.7315	9.4778	7.0874	5.7228
H error mean before correction (m)	−894.4769	−361.2560	−152.5477	−81.1574
H error std before correction (m)	64.5196	48.7740	35.4394	27.3698
β_{ref} error mean after correction (°)	−0.2709	−0.2698	−0.2642	−0.2639
β_{ref} error std after correction (°)	0.3584	0.2617	0.2104	0.1638
R_{ref} error mean after correction (m)	7.1213	−7.0118	−6.0173	5.0005
R_{ref} error std after correction (m)	13.7174	9.4093	7.0641	5.6580
H error mean after correction (m)	−45.0036	−44.4698	−43.1953	−43.1188
H error std after correction (m)	59.5077	43.4315	34.9951	27.5690

4.1.2. Multi-Beams

This section presents surface target echo simulations for the multi-beams modes to verify the aircraft altitude estimation performance. The geometric parameters for the sequential and cyclic four-beams modes from Tables 1 and 2 are continuously adopted. The simulated scene follows a Rayleigh distribution, and the antenna pattern is shown in Figure 8.

It can be seen from (130) that the SNR is inversely proportional to R^3. In addition, σ_0, ρ_{gr}, and the transmission loss in L_Σ also vary with the incidence angle. In the revised

simulation, these variations are included: σ_0 is modeled as a function of the local incidence angle using the empirical relation $\sigma_0(\theta) = \sigma_0(0) + k_\sigma\theta$ with $k_\sigma = -0.15$ dB/deg for typical land scenes, and ρ_{gr} is calculated from the range resolution and the local incidence angle θ (θ and β are complementary). The SNR of each beam is calculated from (130) using the system parameters in Table 13 and the beam-specific slant range and incidence angle. The resulting SNR values of beam I to beam IV for the two multi-beam modes are listed in Tables 15 and 16, respectively. These values are not arbitrary; they are derived from the radar equation and the actual geometry.

Table 15. SNR of the four beam positions after range pulse compression in the distributed target simulation for the sequential multi-beam mode.

Beam Number	I	II	III	IV
Slant range R_i (km)	15	13	11	9
Grazing angle β_i (°)	15.47	17.87	21.21	26.03
Backscattering coefficient σ_0 (dB)	−15.0	−15.4	−15.8	−16.5
SNR (dB)	8.75	10.61	12.76	15.40

Note: The SNR values are calculated from (130) using the system parameters in Table 13, with the beam-specific slant range, incidence angle, and incidence-angle-dependent σ_0.

Table 16. SNR of the four beam positions after range pulse compression in the distributed target simulation for the cyclic multi-beam mode.

Beam Number	I	II	III	IV
Slant range R_i (km)	11	13.7	13.2	10.3
Grazing angle β_i (°)	21.3	17.0	17.6	22.8
Backscattering coefficient σ_0 (dB)	−15.8	−15.3	−15.4	−16.1
SNR (dB)	12.76	9.89	10.44	13.64

Note: The SNR values are calculated from (130) using the system parameters in Table 13, with the beam-specific slant range, incidence angle, and incidence-angle-dependent σ_0.

Monte Carlo simulations are performed. For each beam position, 64,000 echoes are generated, with every 64 PRT grouped as one dataset for aircraft altitude estimation. Each dataset is processed independently to estimate the aircraft altitude, with a data acquisition time of 32 ms per dataset. In the simulation, Δ_{β_1} is modeled as a Gaussian random variable with unit variance. The 3σ errors of variations in the grazing angle δ_{i1} and the aircraft altitude h_{i1} are listed in Table 17.

Table 17. Errors in the variations in grazing angle and aircraft altitude for the multi-beam mode.

Mode	Variation in the Grazing Angle $\boldsymbol{\delta_{i1}}$ (°)	Variation in the Aircraft Altitude $\boldsymbol{h_{i1}}$ (m)
Sequential four-beam	0.05	10
Cyclic four-beam	0.02	5

For the sequential four-beams, Table 18 presents the estimated beam-center slant ranges obtained from the zero-depth position of the difference channel. The maximum deviation is approximately 10 m, and the standard deviation decreases as the slant range increases. Figure 10a shows the estimated altitude for each dataset, with an average deviation of −0.29 m and a standard deviation of 9.85 m.

Table 18. Statistical results of beam-center slant range estimation error for the sequential four-beam mode in the distributed target simulation.

Beam Number	I	II	III	IV
Beam-center slant range deviation (m)	−4.41	−9.69	−0.76	9.80
Beam-center slant range standard deviation (m)	10.23	7.45	3.72	2.00

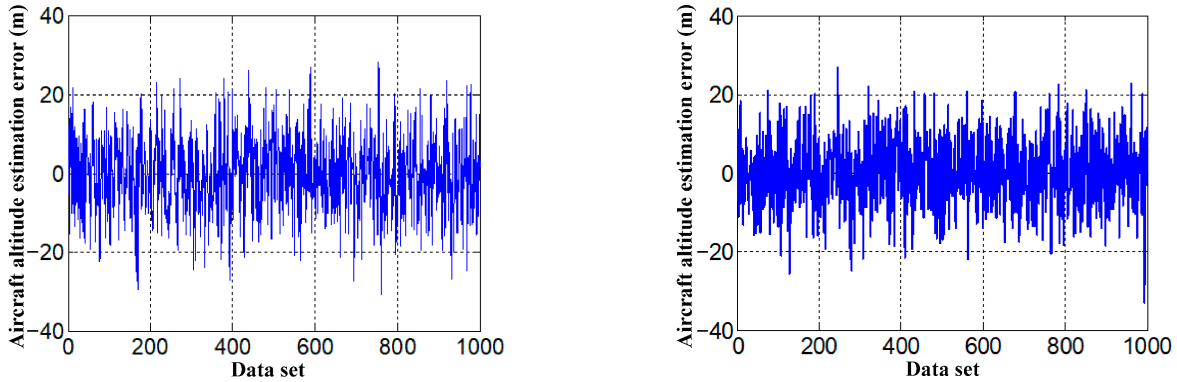


Figure 10. Aircraft altitude estimation error for each dataset in the distributed target simulation: (**a**) sequential four-beam mode; and (**b**) cyclic four-beam mode.

For the cyclic four-beams, Table 19 presents the corresponding results. The maximum deviation is approximately 7 m, and the standard deviation also decreases with the slant range. Figure 10b shows the estimated altitude for each dataset, with an average deviation of −0.20 m and a standard deviation of 8.82 m. Both methods achieve a high estimation accuracy.

Table 19. Statistical results of beam-center slant range estimation error for the cyclic four-beam mode in the distributed target simulation.

Beam Number	I	II	III	IV
Beam-center slant range deviation (m)	−5.18	−6.27	−6.67	−1.53
Beam-center slant range standard deviation (m)	3.49	7.81	7.24	3.37

The simulation results demonstrate that the aircraft altitude estimation accuracy based on the pitch sum with difference channels is highly sensitive to the grazing angle accuracy. With a 1° grazing angle error, the altitude estimation error can reach tens of meters. In contrast, the multi-beam modes effectively eliminate the impact of the grazing angle error. When the error in the grazing angle variation is small, high-accuracy altitude estimation is achieved.

4.2. Real Data

To further validate the feasibility of the multi-beam-based aircraft altitude estimation method, the processing results of airborne measured data are presented below, covering both the sequential and cyclic four-beam approaches. In all measured-data results reported in this section, the angle-bias correction is applied to the sum–difference channel angle measurements prior to curve fitting. Therefore, the resulting altitude errors inherently include the effect of this correction.

The reference altitude used in the measured-data validation was provided by an airborne dual-frequency geodetic-grade GPS receiver, operating in post-processed kinematic (PPK) mode. The update rate was 10 Hz, and the post-processed vertical positioning accuracy was about 3 cm (1σ). The GPS antenna was mounted on the top of the fuselage, and the lever-arm offset between the GPS antenna phase center and the radar antenna phase center was measured and compensated before comparison. The GPS ellipsoidal altitude was converted to the local orthometric altitude using the EGM2008 geoid model, consistent with the altitude datum used by the radar. The GPS and radar clocks were synchronized by a 1PPS signal, with a synchronization error of less than 1 ms. For each dataset, the GPS reference altitude at the radar acquisition center was obtained by linear interpolation of the GPS samples within the 32 ms acquisition window.

The uncertainty of the GPS reference altitude is

$$\sigma_{\text{ref}} = \sqrt{\sigma_{\text{GPS}}^2 + (V\sigma_t)^2 + \sigma_{\text{datum}}^2}, \tag{131}$$

where $\sigma_{\text{GPS}} \approx 0.03$ m is the GPS vertical accuracy, V is the platform velocity, $\sigma_t < 0.001$ s is the time-synchronization error, and $\sigma_{\text{datum}} \approx 0.05$ m is the geoid-conversion uncertainty. For the present parameters ($V = 120 - 225$ m/s), the second term is at most 0.225 m, and

$$\sigma_{\text{ref}} = \sqrt{0.03^2 + 0.225^2 + 0.05^2} \approx 0.23 \text{ m}, \tag{132}$$

which is much smaller than the altitude estimation error reported in Tables 18 and 19 (on the order of a few meters to tens of meters). Therefore, the GPS reference uncertainty does not significantly affect the error statistics.

4.2.1. Sequential Four-Beam

The platform velocity is 120 m/s, and the reference aircraft altitude measured by high-precision GPS is 4992 m. Following the same processing procedure as in the simulations, every 64 pulses are grouped as one dataset for a single aircraft altitude estimation, with a data acquisition interval of 32 ms, yielding a total of 130 datasets. Figure 11 presents the aircraft altitude estimation results obtained by three different methods. Figure 11a–c show the aircraft altitude estimates based on the Doppler centroid, the single-beam pitch sum with difference channels, and the sequential four-beams, respectively. The statistical results for the three methods are given in Table 20. The sequential four-beams method achieves significantly higher accuracy than the other two methods.

Table 20. Statistical results of aircraft altitude estimation errors for different methods.

Method	Mean (m)	Standard Deviation (m)
Doppler centroid	81.88	6.86
Single-beam pitch sum with difference channels	121.24	1.58
Sequential four-beam	−4.66	2.31

The Doppler-centroid-based method indirectly estimates altitude by exploiting the variation in the Doppler centroid with range. Since the data are acquired in a highly squinted sub-aperture mode, the Doppler centroid estimation is significantly affected by non-uniform ground scattering properties. This causes the estimated Doppler variation to deviate from the true values, thereby degrading the altitude estimation accuracy. The altitude estimation error of the single-beam pitch sum with difference channels method is on the order of 120 m. For this method, the grazing angle provided by the INS contains a relatively large error. Assuming a slant range estimation error of 10 m, the INS-provided grazing angle error is

inferred to be approximately 0.7°. The sequential four-beam method effectively eliminates the large common grazing-angle bias among beams. With the fitting intervals in Table 21 and the angle-bias correction in (14), the altitude error mean is −4.66 m and the standard deviation is 2.31 m, corresponding to approximately 0.09% and 0.05% of the GPS reference altitude (4992 m), respectively.

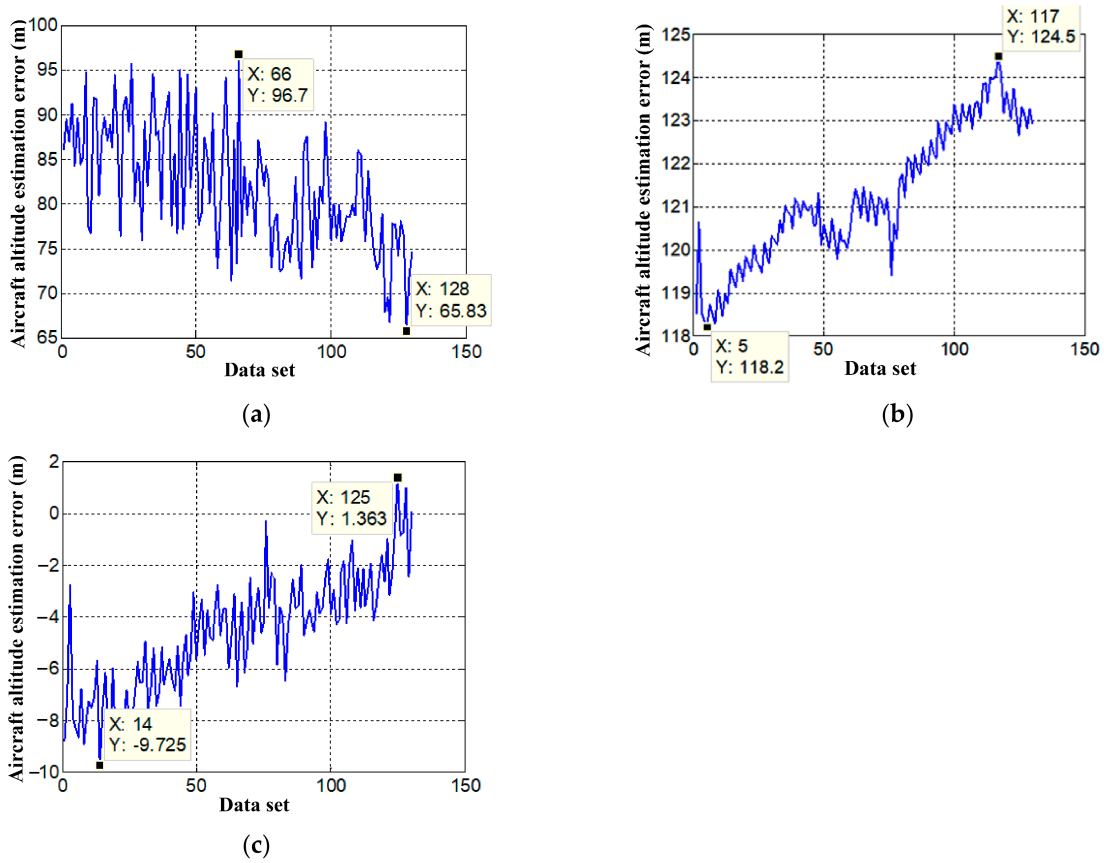


Figure 11. Estimation errors of different altitude estimation methods: (**a**) Doppler centroid method; (**b**) single-beam pitch sum with difference channels method; and (**c**) sequential four-beam method.

Table 21. Selected curve-fitting intervals for the sequential four-beam measured data.

Beam	Zero-Crossing Center $R_{i,c}$ (km)	Half-Window L_i (km)	Selected Interval (km)
Beam I	10.95	0.75	10.20–11.70
Beam II	9.95	0.75	9.20–10.70
Beam III	8.95	0.75	8.20–9.70
Beam IV	7.95	0.75	7.20–8.70

Figure 12 presents the measured difference-over-sum ratio curves for the four beams using the sequential four-beam method. The blue curves represent the actual angle measurement results. As shown in Figure 12a, the angle measurements near the beam center vary smoothly with range, whereas those away from the beam center exhibit severe fluctuations. Comparing different beams reveals that, as the beam-center slant range decreases, the stable interval near the beam center becomes narrower. For each beam, the fitting interval is selected using the procedure in Section 2.2.3. The half-window is bounded by the theoretical constraint $L \leq 0.75$ km ($|c_3/c_2| \approx 0.1$ km^{-1}; with $\eta_L = 7.5\%$). The selected intervals are listed in Table 21, and the red segments in Figure 12 indicate the interval endpoints. This fitting

subsequently enables the estimation of the beam-center slant range. Combined with the inter-beam grazing angle and altitude variations provided by the INS, the aircraft altitude is then estimated.

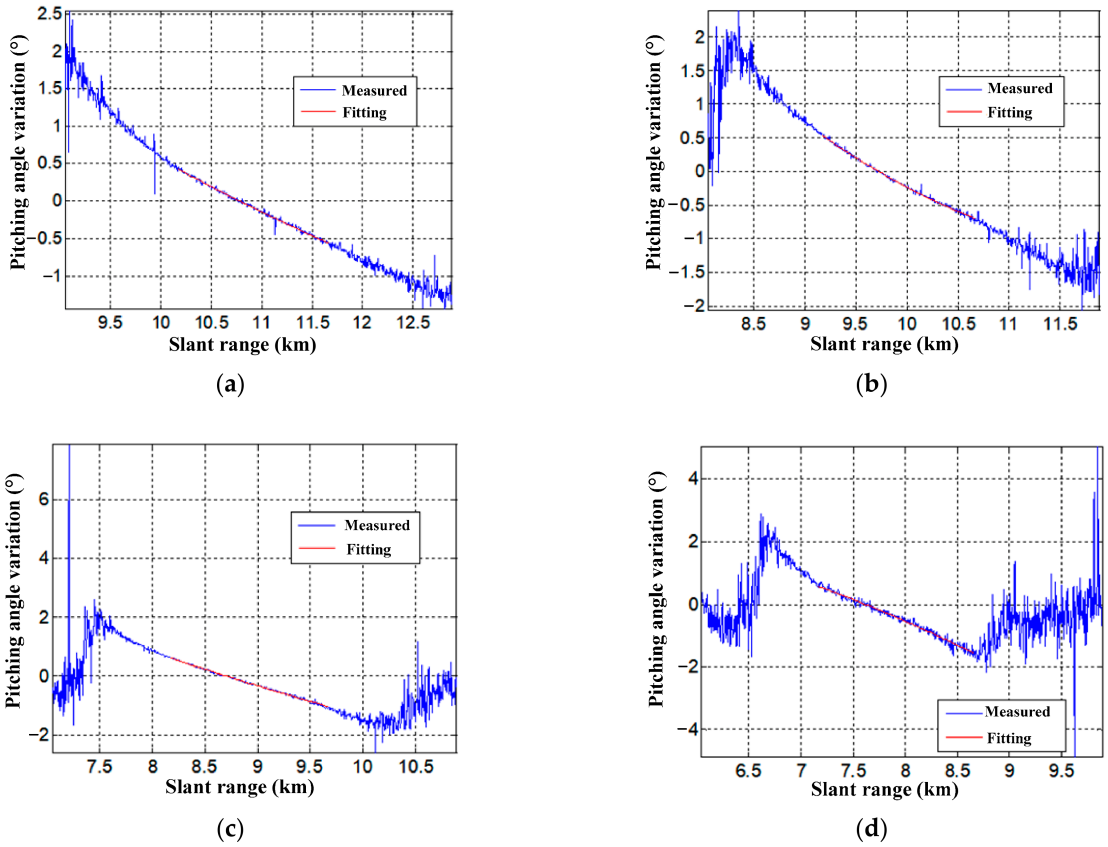


Figure 12. Measured angle curves for the four beam positions of the sequential four-beams mode: (**a**) beam I; (**b**) beam II; (**c**) beam III; and (**d**) beam IV.

4.2.2. Cyclic Four-Beam

The platform velocity is 225 m/s, and the reference aircraft altitude measured by high-precision GPS is 10942 m. Following the same processing procedure as in the simulations, every 64 pulses are grouped as one dataset for a single aircraft altitude estimation, with a data acquisition interval of 32 ms. It should be noted that, unlike the 130 datasets available for the sequential four-beams mode, only two datasets are available for the cyclic four-beam mode. The data processing results for the three altitude estimation methods are given in Table 22. For the two available datasets, the cyclic four-beam method provides a lower altitude estimation error than the other two methods. However, this result should be regarded as preliminary because the sample size is too small to establish statistical robustness.

Similar to the sequential four-beam measured data, the Doppler-centroid-based method with cyclic data is also significantly affected by non-uniform ground scattering properties, since the data are acquired in a highly squinted sub-aperture mode. The estimation error of the single-beam based method is on the order of 225 m. Assuming a slant range estimation error of 10 m, the INS-provided grazing angle bias is inferred to be approximately 0.5°. The cyclic four-beam-based method effectively eliminates the large common grazing-angle bias among beams. Because the angle measurement is based on the ratio of the difference- and sum-channel data, the mean scattering coefficients of different patches are canceled in the ratio and do not directly bias the angle estimate. The patch-to-patch scattering difference mainly changes the SNR and, hence, the angle measurement variance of each beam, which

is handled by the weighted least squares in (63). The residual within-patch scattering non-uniformity is suppressed by the per-beam correction in (14) and by excluding range cells with abrupt scattering changes. With these measures, the altitude estimation accuracy is within 15 m for both datasets. Because only two measured datasets are available, these results are preliminary.

Table 22. Estimation errors for different altitude estimation methods.

Method	Estimation Error of the First Dataset (m)	Estimation Error of the Second Dataset (m)
Doppler centroid	−64.52	−83.17
Single-beam pitch sum with difference channels	226.44	225.62
Cyclic four-beam	14.10	−3.20

Figure 13 presents the measured difference-over-sum ratio curves for the four beams using the cyclic four-beam method. The blue curves represent the actual angle measurement results. For the cyclic four-beam data, the fitting interval of each beam is selected independently using the same procedure in Section 2.2.3. The half-window is 1.25–1.40 km, which satisfies the theoretical bound $L \leq 1.3$ km ($|c_3/c_2| \approx 0.038$ km^{-1}; with $\eta_L = 5\%$) at the larger slant range of the cyclic geometry. The selected intervals are listed in Table 23, and the red segments in Figure 13 indicate the interval endpoints. This fitting subsequently enables the estimation of the beam-center slant range. Combined with the inter-beam grazing angle and altitude variations from the INS, the aircraft altitude is estimated.

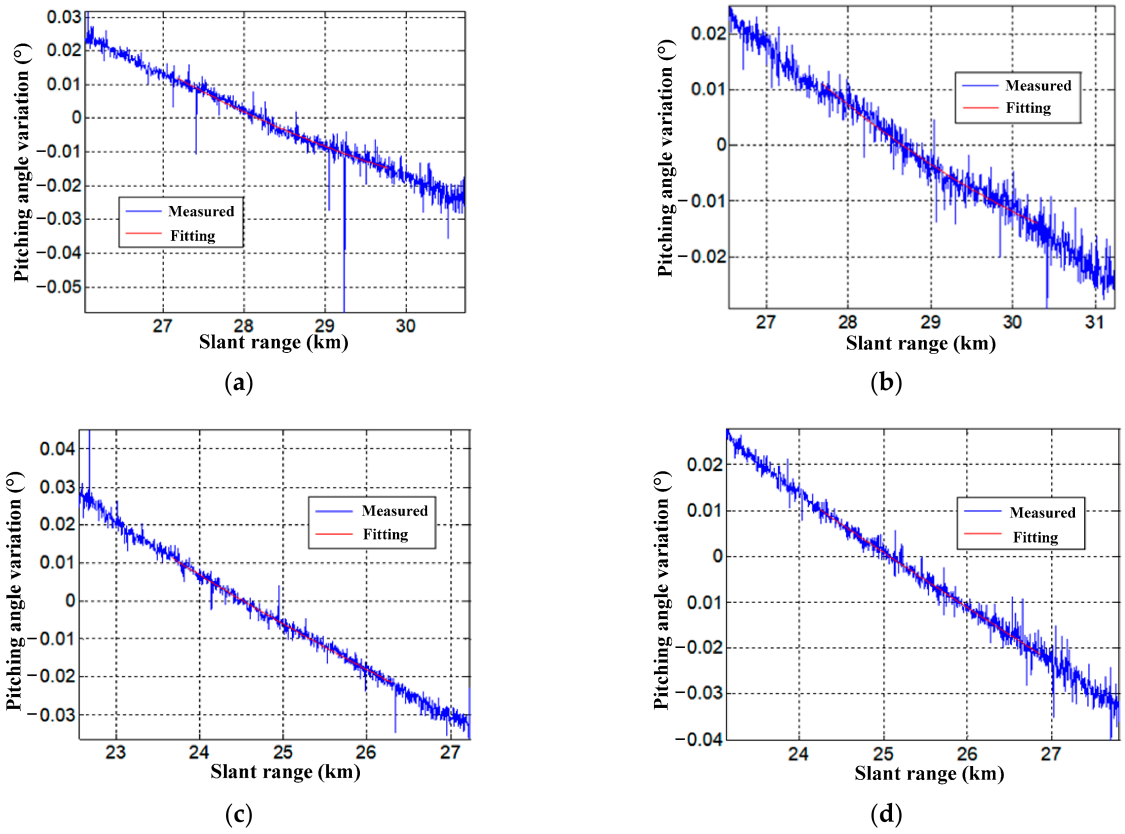


Figure 13. Measured angle curves for the four beam positions of the cyclic four-beams mode: (**a**) beam I; (**b**) beam II; (**c**) beam III; and (**d**) beam IV.

Table 23. Selected curve-fitting intervals for the cyclic four-beam measured data.

Beam	Zero-Crossing Center $R_{i,c}$ (km)	Half-Window L_i (km)	Selected Interval (km)
Beam I	28.50	1.30	27.20–29.80
Beam II	29.00	1.30	27.70–30.30
Beam III	25.00	1.30	23.70–26.30
Beam IV	25.50	1.30	24.20–26.80

5. Discussion

To assess the applicability of the proposed multi-beam-based method, this section compares it with several existing aircraft altitude measurement methods. In practice, the advantages and disadvantages of each method should be fully considered based on the specific scenario to select the most appropriate approach. Table 24 summarizes the advantages and disadvantages of these different methods.

Table 24. Advantages and disadvantages of the different aircraft altitude estimation methods.

Method	Advantage	Disadvantage
Radar altimeter	1. Estimation based entirely on echoes, independent of inertial navigation; 2. Simple principle and ease of real-time processing.	1. Requires a separate altitude measurement antenna, increasing system complexity; 2. Cannot directly measure the altitude of the beam illumination area; 3. Accuracy is susceptible to the beam's ground footprint size.
Doppler centroid	1. Estimation based entirely on echoes, independent of inertial navigation; 2. Precision close to the Cramer–Rao lower bound.	1. Inapplicable to broadside mode; 2. Not directly applicable during beam rotation or diving motion.
Autofocus or phase calibration	1. Applicable to various modes (flat flight, diving, broadside, squint); 2. Less affected by non-uniform scene scattering.	1. Accuracy depends on image focusing quality; 2. Requires iterative processing, making it unsuitable for real-time applications.
Pitch sum with difference channels	1. Applicable to various modes (flat flight, diving, broadside, squint); 2. Less affected by non-uniform scene scattering.	1. Estimation results are biased during beam rotation around the center; 2. Requires precise antenna pattern calibration.
Multi-beams	1. Applicable to various modes (flat flight, diving, broadside, squint); 2. Less affected by non-uniform scene scattering.	1. Requires relative altitude and grazing angle variations from the INS; 2. Beam positions cannot be too close, and beam design is complex.

Radar-altimeter-based altitude estimation relies on the echo mainlobe and synthetic aperture measurement. This method is simple in principle and suitable for real-time processing. However, at high altitudes, the beam's ground footprint becomes considerably large, which degrades measurement accuracy. Furthermore, a separate altitude measure-

ment antenna must be installed for the radar altimeter, significantly increasing the system complexity. In addition, the radar altimeter only measures the altitude directly beneath the platform. If the beam-center slant range of the SAR is relatively large, significant differences may exist between the altitude of the beam illuminated area and the area directly below the platform. Consequently, this inevitable altitude error degrades geometric correction accuracy, rendering the direct use of a radar altimeter ineffective.

For the Doppler-centroid-based method, the aircraft altitude is estimated from the variation in the Doppler centroid with the slant range. However, in broadside mode, the Doppler centroid is always zero, making this method inapplicable. The estimation accuracy improves as the squint angle increases. Furthermore, the Doppler centroid model is relatively simple. In practice, the beam may rotate around its center, or the platform may have a diving velocity, as shown in Figure 14. In such cases, the relationship between the Doppler centroid and slant range becomes more complex, and the method in [16] cannot be directly applied. In addition, if the scene scattering is non-uniform, the Doppler centroid estimation may be erroneous [26], reducing altitude accuracy. This effect is particularly pronounced in the sub-aperture imaging mode of highly maneuverable SAR platforms.

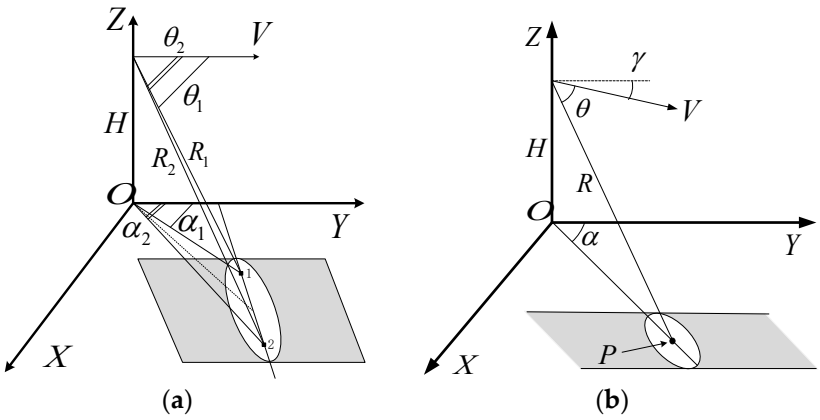


Figure 14. Special geometric configurations: (**a**) beam rotation around the center; and (**b**) platform diving.

Autofocusing or phase-calibration-based altitude estimation operates in both broadside and squint modes, as well as during diving motion. The estimation accuracy is less affected by non-uniform scene scattering. These methods typically require one or multiple images and use iterative processing to accurately estimate altitude-related errors or the altitude itself. Consequently, the estimation accuracy depends on the image focusing quality, making them unsuitable for real-time processing, especially for high-speed diving SAR.

The single-beam pitch sum with difference channels method is also applicable to the broadside, squint, and diving scenarios. However, if the beam rotates around its center, the targets within the same range gate have different pitch-angle deviations. Since only the average pitch angle is estimated, an error is introduced into the slope of the angle-versus-range curve, ultimately degrading altitude accuracy. Because this method estimates the aircraft altitude based on the sum-to-difference channel ratio, it effectively suppresses the influence of non-uniformity scene scattering. In addition, this method requires a more precise calibration of the antenna pattern and is highly sensitive to channel inconsistencies and slope measurement accuracy. Furthermore, the terrain-undulation analysis in Section 2.1 shows that the single-beam method is sensitive to surface elevation variation. When the observation area has a strong terrain relief, the terrain correction in (2) or an external digital elevation model should be used. The multi-beam mode partially

suppresses the common-mode terrain error because the beams observe nearby footprints, but patch-to-patch elevation differences still need to be considered in the cyclic mode.

The multi-beam-based altitude estimation method also operates in broadside and squint modes, as well as during diving motion. Provided that the beam rotation around the center is not excessively large, this method remains applicable. Its accuracy is less affected by non-uniform scene scattering. However, this method requires the INS to provide relative variations in the aircraft altitude and grazing angle between beam positions; thus, the altitude accuracy depends on the precision of these variations. In addition, the grazing angles of different beam positions cannot be too close; otherwise, the solution to (36) becomes highly sensitive to parameter error, leading to large altitude estimation errors. To ensure the independence of the equations in (36) for the sequential four-beam method, the time intervals between beam positions should be as large as possible. However, this increases INS measurement errors, resulting in larger altitude errors. Because the beam switching time in the cyclic four-beam method is much shorter than the beam interval in the sequential method, the relative variations in altitude and angle are theoretically more accurate. This also provides clear advantages in real-time performance. In summary, the design of beam positions for multi-beam altitude estimation must balance many factors, including INS accuracy, grazing angle variation, and real-time requirements. The sensitivity analysis in Section 3.1.1 shows that the sequential multi-beam mode is almost insensitive to prior ground-footprint elevation errors because the common-mode error is canceled in the differential Earth-curvature term. In contrast, the cyclic multi-beam mode directly transfers patch elevation errors to the altitude estimate. Therefore, for the cyclic mode, the ground-footprint elevation should be provided by a digital elevation model or a local reference with an accuracy comparable to the required altitude accuracy. For the sequential multi-beam mode, the beam time interval is determined by the beam spacing and the platform velocity, and the INS relative-error accumulation grows with this interval. There exists an optimal beam spacing that balances geometric sensitivity and INS error accumulation. If the required altitude accuracy cannot be met within the real-time constraint, the cyclic multi-beams mode should be used, as its shorter beam switching time makes INS error accumulation negligible. For the cyclic multi-beam mode, patch-to-patch scattering differences do not directly bias the angle estimate because the mean scattering coefficient is canceled in the difference-over-sum ratio. Its influence appears mainly as a change in the SNR, and, hence, the angle measurement variance in each beam, which is handled by the weighted least squares in (63). The residual within-patch scattering non-uniformity is suppressed by the per-beam correction in (14) and by range-cell selection.

Data collected using the traditional strip-map SAR mode can be applied to both the Doppler-centroid-based method and the pitch sum with difference channels method. Due to the limitations of these two estimation methods, the multi-beam estimation results are generally superior. In practice, the advantages and disadvantages of each method must be evaluated based on the specific scenario to select the most appropriate approach.

A limitation of this study is that the cyclic multi-beam mode has only been tested on two measured datasets, whereas the sequential mode has 130 datasets. The two cyclic datasets provide encouraging preliminary results, but they are insufficient to fully demonstrate the robustness of the algorithm or to establish statistically meaningful performance bounds. The current cyclic results should, therefore, be regarded as a preliminary feasibility validation. In future work, we will collect more flight measurements under different trajectories, terrain conditions, and scattering scenarios to verify the robustness and generality of the cyclic multi-beam method. The measured data will also be expanded to typical scenarios such as sea-level conditions. The processing time in Section 3.5 is a theoretical estimate from the computational complexity, not a hardware measurement. The actual processing time

depends on the instruction-level parallelism, memory access, and implementation details of the target processor. Hardware-in-the-loop testing on an embedded airborne processor has not yet been conducted and will be carried out in future work. In addition, the azimuthal sum with difference channel data will be studied for angle measurement, which provides another independent real-time altitude estimation method that is less susceptible to non-uniform scene scattering.

6. Conclusions

This article proposes multi-beam altitude estimation methods based on radar echoes for adaptive real-time aircraft altitude estimation. According to the beam position design and data acquisition manner, the method is divided into sequential multi-beam and cyclic multi-beam modes. This paper describes the estimation principles and processes of both modes. Their validity is verified through simulations and measured data processing. The estimation accuracy and applicable range of each method are analyzed and compared. A complete covariance propagation is established for error analysis, and analytical design formulae for beam positions are derived. The processing time is also estimated to evaluate the real-time performance.

To achieve adaptive real-time altitude estimation via multi-beams, the grazing angle difference between beam positions should be as large as possible. The estimation accuracy is affected by several factors. These include grazing angle variation errors, aircraft altitude variation errors, INS relative-error accumulation, and prior ground-footprint elevation errors.

Future work will use the azimuthal sum with difference channel data for angle measurement. This approach eliminates the energy modulation caused by non-uniform scene scattering. It will provide an independent real-time altitude estimation method that is insensitive to non-uniform scattering intensity.

Author Contributions: Conceptualization, Z.Z. and N.Z.; methodology, Z.Z. and W.W.; software, Z.Z.; validation, Z.Z. and X.H.; formal analysis, Z.Z. and X.H.; investigation, Z.Z. and B.H.; resources, Z.Z. and B.H.; data curation, Z.Z.; writing—original draft preparation, Z.Z.; writing—review and editing, Z.Z., N.Z., W.W., X.H. and B.H.; visualization, Z.Z.; supervision, Z.Z. All authors have read and agreed to the published version of the manuscript.

Funding: This research received no external funding.

Data Availability Statement: Restrictions apply to the availability of these data. The measured data used in this study were self-developed and are subject to confidentiality agreements. They are available from the corresponding author upon reasonable request and with the permission of the relevant authorities.

Conflicts of Interest: The authors declare no conflicts of interest.

Abbreviations

The following abbreviations are used in this manuscript:

SAR	Synthetic aperture radar
INS	Inertial Navigation System
GPS	Global Positioning System
MFLOP	Million Floating-point Operation
GFLOP	Giga Floating-point Operation
SNR	Signal-to-Noise Ratio
RMSE	Root Mean Square Error

References

1. Singh, A.P.; Singh, V. A Novel Hybrid Autofocusing Technique for Compressive Sensing-Based Through-the-Wall Radar Imaging with Synthetic Aperture Radar System. *IEEE Sens. Lett.* **2025**, *9*, 3506604. [CrossRef]
2. Liu, Y.; Tao, M.; Shi, T.; Wang, J.; Wang, J.; Mao, X. Sub-Aperture Polar Format Algorithm for Curved Trajectory Millimeter Wave Radar Imaging. *IEEE Trans. Radar Syst.* **2024**, *2*, 67–83. [CrossRef]
3. Chen, X.; Dong, Z.; Zhang, Z.; Tu, C.; Yi, T.; He, Z. Very High Resolution Synthetic Aperture Radar Systems and Imaging: A Review. *IEEE J. Sel. Top. Appl. Earth Obs. Remote Sens.* **2024**, *17*, 7104–7123. [CrossRef]
4. Shimada, M. Ortho-Rectification and Slope Correction of SAR Data Using DEM and Its Accuracy Evaluation. *IEEE J. Sel. Top. Appl. Earth Obs.* **2010**, *3*, 657–671. [CrossRef]
5. Xing, M.; Jiang, X.; Wu, R.; Zhou, F.; Bao, Z. Motion Compensation for UAV SAR Based on Raw Radar Data. *IEEE Trans. Geosci. Remote Sens.* **2009**, *47*, 2870–2883. [CrossRef]
6. Li, Y.; Liu, C.; Wang, Y.; Wang, Q. A Robust Motion Error Estimation Method Based on Raw Data. *IEEE Trans. Geosci. Remote Sens.* **2012**, *50*, 2780–2790. [CrossRef]
7. Long, T.; Liu, L.; Ding, Z. Strategy of Doppler centroid estimation in synthetic aperture radar. *IET Radar Sonar Navig.* **2011**, *5*, 279–287. [CrossRef]
8. Long, T.; Li, Y.; Ding, Z.; Liu, L. Interpolation method for geometric correction in highly squint synthetic aperture radar. *IET Radar Sonar Navig.* **2012**, *6*, 620–626. [CrossRef]
9. Kreyenkamp, O.; Klemm, R. Doppler compensation in forward-looking STAP radar. *IEEE Proc. Radar Sonar Navig.* **2001**, *148*, 253–258. [CrossRef]
10. Fitzgerald, K. Targeting the enemy: Radar, radio control and inertial-guidance systems helped improve the accuracy of both offensive and defensive weaponry. *IEEE Spectr.* **1987**, *24*, 42–49. [CrossRef]
11. Li, J.; Fan, X.; Wang, C.; Bao, H.; Xiao, Y. Accuracy assessment of GPS navigation augmented by SAR and LiDAR-derived digital elevation models. *Int. J. Digit. Earth* **2014**, *8*, 1007–1022. [CrossRef]
12. Nassar, S. Improving the Inertial Navigation System (INS) Error Model for INS and INS/DGPS Applications. Ph.D. Thesis, University of Calgary, Calgary, AB, Canada, 2003.
13. Newton, G. Inertial-Guidance Limitations Imposed by Fluctuation Phenomena in Gyroscopes. *Proc. IRE* **1960**, *48*, 520–527. [CrossRef]
14. Duan, M.; Lu, Y.; Wang, Y.; Liu, G.; Tan, L.; Gao, Y.; Li, F.; Jiang, G. Above Ground Level Estimation of Airborne Synthetic Aperture Radar Altimeter by a Fully Supervised Altimetry Enhancement Network. *Remote Sens.* **2023**, *15*, 5404. [CrossRef]
15. Wang, Q.; Jing, W.; Liu, X.; Huang, B.; Jiang, G. Signal Processing and Waveform Re-Tracking for SAR Altimeters on High Mobility Platforms with Vertical Movement and Antenna Mis-Pointing. *Sensors* **2023**, *23*, 9266. [CrossRef] [PubMed]
16. Zeng, T.; Li, Y.; Ding, Z.; Liu, L.; Zou, F. Estimation of Aircraft Altitude Based on Squint Mode SAR Data. *IEEE Geosci. Remote Sens. Lett.* **2015**, *12*, 135–139. [CrossRef]
17. Ash, J. An Autofocus Method for Backprojection Imagery in Synthetic Aperture Radar. *IEEE Geosci. Remote Sens. Lett.* **2012**, *9*, 104–108. [CrossRef]
18. Cantalloube, H.; Nahum, C. Multiscale Local Map-Drift-Driven Multilateration SAR Autofocus Using Fast Polar Format Image Synthesis. *IEEE Trans. Geosci. Remote Sens.* **2011**, *49*, 3730–3736. [CrossRef]
19. Ponce, O.; Iraola, P.; Scheiber, R.; Reigber, A.; Moreira, A.; Aguilera, E. Polarimetric 3-D Reconstruction from Multicircular SAR at P-Band. *IEEE Geosci. Remote Sens. Lett.* **2014**, *11*, 803–807. [CrossRef]
20. Tebaldini, S.; Alessandro, M.; Banda, F.; Prati, C. Tomographic-quality phase calibration via phase center double localization. In *2013 IEEE International Geoscience and Remote Sensing Symposium—IGARSS*; IEEE: New York, NY, USA, 2014; pp. 89–92.
21. Tang, S.; Zhang, L.; Guo, P.; Zhao, Y. An Omega-K Algorithm for Highly Squinted Missile-Borne SAR with Constant Acceleration. *IEEE Geosci. Remote Sens. Lett.* **2014**, *11*, 1569–1573. [CrossRef]
22. Xu, H.; Gao, J.; Li, L. A variable PRF imaging method for high squint diving SAR. *Prog. Electromagn. Res.* **2013**, *135*, 215–229. [CrossRef]
23. Li, H.; Wang, Y.; Luo, X. Tree altitude Estimation at Plateau Mountains, Northwestern Sichuan, China Using Dual Pol-InSAR Data. In Proceedings of the 2016 IEEE International Geoscience and Remote Sensing Symposium (IGARSS), Beijing, China, 10–15 July 2016.
24. Li, L.; Yang, W.; Zhou, Z.; Ding, Z. Aircraft altitude estimation method based on multi beams pitching sum and difference channels for SAR. *J. Eng.* **2019**, *19*, 5780–5784. [CrossRef]

25. Sherman, S.; Barton, D. *Monopulse Principles and Techniques*; Artech House: Norwood, MA, USA, 2011.
26. Madsen, S. Estimating the Doppler centroid of SAR data. *IEEE Trans. Aerosp. Electron. Syst.* **1989**, *25*, 134–140. [CrossRef] [PubMed]

Disclaimer/Publisher's Note: The statements, opinions and data contained in all publications are solely those of the individual author(s) and contributor(s) and not of MDPI and/or the editor(s). MDPI and/or the editor(s) disclaim responsibility for any injury to people or property resulting from any ideas, methods, instructions or products referred to in the content.